ADDIS ABABA UNIVERSITY
SCHOOL OF GRADUATE STUDIES
FACULTY OF SCIENCE
DEPARTMENT OF GEOLOGY AND GEOPHYSICS

INTEGRATED GEOPHYSICAL METHODS TO INVESTIGATE THE GEOLOGICAL STRUCTURES AND HYDROSTRATIGARAPHIC UNIT OF THE AYNALEM AREA, SOUTHEAST MEKELLE

A THESIS PRESENTED TO THE SCHOOL OF GRADUATE STUDIES OF ADDIS ABABA UNIVERSITY IN PARTIAL FULFILLMENT OF THE REQUIREMENTS FOR THE DEGREE OF MASTER OF SCIENCE IN GEOPHYSICS

BY:
BERHANU GEBREGZIABHER

ADVISOR: Dr. TILAHUN MAMMO

June 2003

ACKNOWLEDGEMENT

At every step during the work of this research, vital assistance was provided by a number of people and institutions, whose help is acknowledged with gratitude (with apologies to anyone inadvertently omitted).

Before all I am very grateful to my advisor Dr. Tilahun Mammo, for the most important guidance and his valuable and constructive advice both in the field and during compilation of this thesis.

I would like to express my deep gratitude to Mekelle University particularly to Dr. Kurkura Kebeto (Dean for the Faculty of Science and Technology) and Ato Tirufat H.Mariam (Department Head of Applied Geology) for providing me car and the very expensive geophysical instruments during the fieldwork.

Many thanks go to EZANA Mining Development Plc. for allowing me their Magnetometer and unforgettable thanks to Ato Paulos for his help during the fieldwork. I would like also to forward my respected thanks to REST for their willing to allow me their Terrameter.

For the different materials and information I received, great thanks to Mekelle Water Supply Service Office and to my friends Abdelwassie Hussein, G.Medhin Berhane, and Samuel Yehdego. And I couldn't pass with out mentioning the help from Dr. Dagnachew Leggese in helping me digitizing some of the maps.

Last but not least I would like to appreciate my parents and to my friends both in Mekelle (during the fieldwork) and in Addis (during data processing) for their help and encouragements.

TABLE OF CONTENTS

LIST OF FIGURES

ABSTRACT

Water is life. Without water life cannot exist. This integrated geophysical investigation in conjunction with geological survey is conducted in exploration for underground water supplies.

Surface lithologic and structural mapping, refraction seismic, magnetic and electrical resistivty data were acquired for a project in the Aynalem area 5 km southeast Mekelle to aid in the search for ground water supplies.

The geology of the area consisted of the Tertiary Dolerite dykes and sills intruded into a soft rock sedimentary terrain of Mesozoic age. From the oldest to the youngest the main rock units in the study area are; the limestone rock unit, the shale-limestone-marl intercalation unit, and the Dolerite rock units. The geologic work helps to select the appropriate profile directions for the geophysical survey and in the final interpretation of the geophysical results.

The purposes of the geophysical surveys were to outline fractures and faults so as to locate possible water saturated zones and give an indication of lithologic differences. Accordingly, geologic structures such as fractures, faults, and geologic boundaries have been identified. In some parts of the study area (on the southeastern part) a depth to the water saturated zone is detected. The shallow subsurface dolerite intrusions are also identified at different depths. Most of the detected fractures and faults are aligned along NW–SE strike directions similar to the regionalstructures.

CHAPTER-1 INTRODUCTION

1.1 Background and Justification

Water is life. Without water life cannot exist. This research work is aimed on the application of integrated geophysical and geologic methods in exploration for underground water supply.

Faced with a general reduction in the amount of the irregular rainfall of the country in general and the study area in particular, the researcher attempted to augment the supplies by studying (exploring) the groundwater resource of the area.

The project area, 5 km Southeast Mekelle near a village called Aynalem, has a number of water wells that have been dug by Water Well Drilling Enterprise in 1992 planning to supply the water requirements of Mekelle town for about twenty years.

The existing population of this town is estimated from 120,000 to 130,000. But as it is known the population is increasing from time to time and these few wells are not enough to secure the growing demands for water. And unfortunately, most of the wells dried up this year. This causes fear and severe shortage in water supply for the increasing population of the town.

Exploration for groundwater in hard rock terrains is beset with difficulties largely due to the fact that the aquifers are limited in their lateral and vertical extent. In the study area, where a large part consists of dykes and sills of the dolerite rock unit, geophysical investigation in conjunction

with geological survey is conducted to map the units and the structures that may be responsible for holding water.

As such the importance of this research work is two fold. Firstly it aims at understanding and mapping the structures (faults and fractures) that serve as conduits for groundwater movement and definitely hold some water. Secondly and consequently it identifies and proposes suitable areas for productive water supply thus make it possible to reduce the risk of drilling dry holes.

1.2 Previous Studies

The area has been studied by a number of researchers. But most of these works focused on geology, hydrogeology, and engineering geology. Only Tesfaye Chernet et al. (1982) and Vernier (1985) conducted an electrical survey for hydro geological investigation to assess the groundwater potential of the Mekelle town. Geological mapping of the Aynalem catchment were done by Abdelwassie Hussein (2000) to investigate the hydrogeology of the Aynalem well fields and for both the Ilala and Aynalem catchments by G.medhin (2002).

1.3 Aim of the present study

The main objectives of this research work are:

1. Mapping the network of dolerite sills and dykes that intrude the sedimentary rock terrain.

2. Mapping the major structural features such as fractures, faults, and geologic boundaries that usually serve as conduits for the circulation of groundwater.

3. Understanding and making clear the role of geologic structures and the dolerite intrusions in the movement and occurrence of groundwater and characterize the aquifer systems.
4. Investigating the problem of some un-functional wells and locating additional drilling sites in the study area.

1.4 Methodology

The methods employed to achieve the objectives of this research were grouped into two as geological and geophysical methods.

Geological mapping was done for a regional assessment of potential fractures and fault zones prior to conducting geophysical survey. Both the stratigraphy of the locality and the orientation of the structures were determined during this stage.

Various geophysical techniques are normally applied to groundwater investigations with some showing more success than others. In this research work refraction seismic, magnetic, and electrical resistivty methods were applied.

1.5 Instruments and materials used

Some of the instruments used during the survey were:

i. A 24-channel digital seismograph (OYO McSEIS-SX) for recording the seismic waves during the refraction seismic survey.
ii. A proton precession IGS-2 magnetometer for conducting the magnetic survey.

iii. ABEM Terrameter SAS 1000 for the electrical resistivty profiling.

iv. GPS for measuring the position of each station and the pumping wells.

v. Compass for measuring the alignments of the fractures and the direction of the survey lines.

The important materials and relevant data used were:

a. Published and unpublished reports for literature review.

b. Aerial photographs with a scale of 1:50,000

c. Topographic maps, south Mekelle and Kwiha sheets, with a scale of 1:50,000.

d. Borehole log data of the wells for calibration of the measurements and results of the surveys.

CHAPTER-2 GENERAL OVERVIEW OF THE AREA

2.1 Location and Extent of the study area

Mekelle, the capital city of the Tigray Regional State, is located about 778 km north of Addis Ababa- the capital city of Ethiopia.

The study area is 5 km southeast of Mekelle around a village called Aynalem. Geographically it is located between $13^0$25’ and $13^0$29’ N latitudes and between $39^0$28’ and $39^0$33’ E longitudes (fig 2.1).

The geophysical survey is made in a restricted area between $13^0$27’02.1” and $13^0$27’59.5” N latitudes and between $39^0$29’54.8” and $39^0$32’19.0” E longitudes. It is a 4.6 by 1.9 km rectangular shape that covers an area of about 8.7 square kilometers.

2.2 Accessibility and Morphology

The main asphalted road from Mekelle to Addis Ababa passes near the northern and eastern sides of the study area. There are accessible driving roads to each pumping wells inside the study area. In addition to this, most of the area is a flat farmland covered by soil and grasses thus giving easy access to every part of the area. All these accessibilities made it easy to transport easily the sensitive geophysical instruments with their cables.

The area is marked with highlands at its northern and southern margins and almost flat at the center. Its elevation varies between 2125 meter on the western side and 2385 meter on top of the southern margin of the valley.

The main river in the area, called Kalamino River, flows from east to west across the central part. This river disappears at & below the Dolerite outcrops and appears below and near the limestone rock outcrops. Most of the tributaries are from the southern margin and flow during the rainy season.

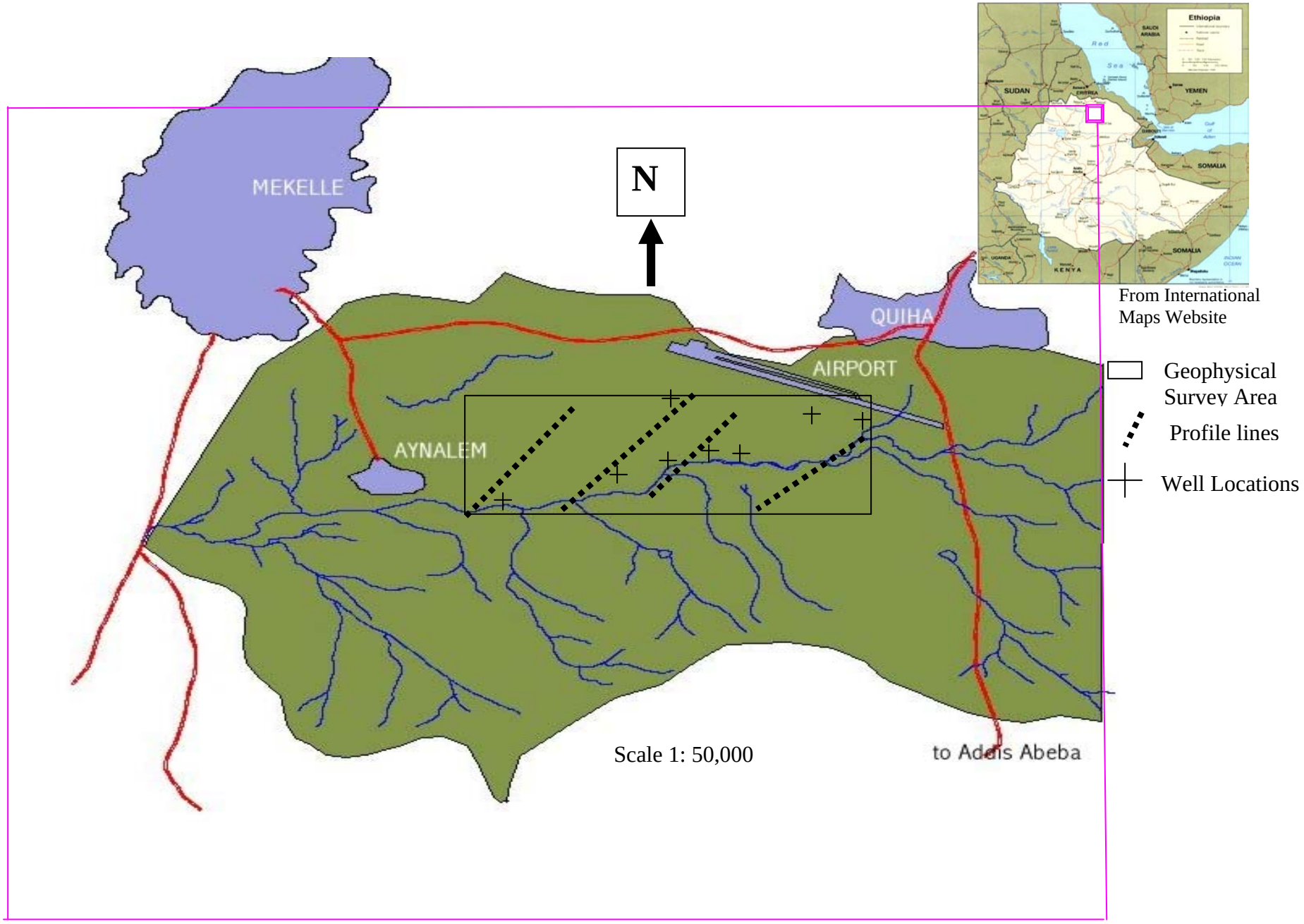

Fig 2.1 Location Map of the study area

CHAPTER-3: GEOLOGY

3.1 Regional geology

3.1.1 Introduction

The Mekelle basin is one of the four Mesozoic sedimentary basins in Ethiopia which is found exposed from Amba-Alage mountain in the southern part up to a small town called Wukro to wards north and from Abiy-Adi on the western part it goes to the east up to the western escarpment of the Ethiopian rift valley.

According to Beyth, 1972; Kazmin, 1975;Bosellini et al, 1997,this sedimentary succession, unconformably overlying the Precambrian basement, forms a nearly circular outlier of 8000 sq. kms in the area around Mekelle.

3.1.2 Stratigraphy

Based on the works of Blandford (1870) and Merla & Minucci (1938), the Mesozoic sedimentary stratigraphy of this basin consists of a lower sandstone unit (the well known Adigrat sandstone), an intermediate carbonate-marly-shaly-gypsiferous unit (the so called Antalo limestone and Agula shale), and an upper sandstone unit (which is called the Amba-Aradom formation).

Based on Arkin et al., 1971; Beyth, 1972; Bosellini et al., 1995; it is well documented by physical field evidence that an angular unconformity separates the Amba-Aradom formation of Mekelle basin from the underlying unit. The same relation ship occurs in western and northern Somalia

and in Kenya (Bosellini, 1992). But according to Dainelli's explanation both the lower and upper sandstone formations are in stratigraphic continuity with the intermediate carbonate-marly succession (Antalo and Agula formations).

The terms Adigrat sandstone and Antalo limestone were assigned by Blandford (1870) and the Amba-Ardom formation by Shumburo (1968). The formational name of Antalo limestone was subsequently extended to Jurassic carbonates of other Ethiopian regions such as the Blue Nile and the Harar plateau and vicinity (Dire-Dawa, Chercher mountains). The so- called Antalo limestone of Mekelle basin is largely constituted of marls and shales, especially around Antalo village (Bosellini et al., 1997).

During the regional mapping of Tigray by the Geological survey of Ethiopia in late 60s, the upper, more marly part of the carbonate succession was separated from the Antalo limestone and named Agula shale (Levitte, 1970;Arkin et al., 1971; Beyth, 1972). According to Bosellini et al., 1997, this term is totally inappropriate because the so-called Agula shale is quite variable in lithology, including some shale but mostly marlstone, coquinoid limestone, quartz sandstone and gypsum. Moreover, the boundary between Antalo and Agula (if any) is transitional and completely arbitrary. Thus Boselline et al. (1997) propose to designate the entire carbonate-marly succession of the former Antalo limestone and Agula shale as a single stratigraphic unit called Antalo super sequence.

The Mekelle Dolerite is found exposed in the Agula shale around Mekelle. According to Levitte (1970), most of which are sills from 0.5-30 meters wide though dykes and small stocks are also common. The whole section is intruded from the basement to Amba-Aradom formation. Levitte

said that the most preferred horizon was the Agula shale formation, which is very soft and has less cover than similarly soft formations that are deeper. This rock type is also found as dykes filling the Mekelle fault.

3.1.3 Structures

According to Beyth (1972), four normal fault belts, running in NW-SE directions, cross the Mekelle outlier. These are the Wukro fault belt, the Mekelle fault belt, the Chelekot fault belt, and Fuicea Mariam fault belt. The Mekelle outlier is therefore composed of three large tilted blocks. Along these fault lines asymmetrical synclines were formed, dipping about 7^0 to NE and 20^0 to SW, and plunging southeast.

Beyth says the Agula shale is mainly exposed along the axis and the main movement along these faults could be post Agula shale and pre-AmbaAradom formation.

These lines are used as fissure dykes by the Mekelle Dolerite. Due Southwest, the tectonic activity of these lines is more effective; there are more faults, and more intrusions of Mekelle Dolerite. All these belts are cut at the east around 40^0 longitudes by the rift valley fault system.

3.1.4 Geologic history

The main geological history, accepted by the majority of geologists who studied the sedimentary succession of Ethiopia, was made by Dainelli (1943). According to Dainelli, the Jurassic transgression came from the southeast, reaching its maximum limit in western Ethiopia and Eritrea during the Kimmeridgian. This transgression deposited a sandy formation called the

Adigrat sandstone, followed by neritic sediments composed mainly of thick limestones the so called Antalo limestone and Agula shale (Antalo super sequence; Bosellini et.al, 1997). Then a regression toward the southeast began after the deposition of the limestone and a near shore upper sandstone facies (Amba-Aradom formation) deposited above the Antalo limestone and Agula shale formations. Tertiary uplift of the Arabian-Ethiopian swell was accompanied by laterization and followed by the eruption of trap volcanics.

According to the literature (Merla & Minucci, 1938;Dainelli, 1943; Beyth, 1972; and Bosellini et al., 1997), the age of the Antalo limestone and Agula shale is oxfordian- kimmeridgian. And the age of the Mekelle Dolerite is Tertiary, probably comagmatic with the trap volcanics (Beyth, 1972).

3.2 Local Geology

3.2.1 Introduction

The study area (around the Aynalem well fields) is almost flat land with some rugged topographic ridges of dolerites that form small hills. The flat land, mostly at the central part, is covered with soil 3 to 7 meters in thickness. This makes difficult to map the lithologic and structural contacts easily.

The area consists of three rock units. From the oldest to the youngest: the limestone, shale-limestone-marl intercalation, and dolerite rock units.

3.2.2 The Limestone Rock Unit

This rock unit is found exposed mainly in the central part of the study area together with thin sandstone beds and also observed on top of the hills overlain by shale-limestone-marl intercalations and underlain by dolerites mainly on the peripheral parts of the study area (fig 3.1).

From the hand specimen this rock is gray to black in color and fine-grained crystalline rock. The sandstone is yellow to white in color.

The limestone is highly fractured and in most places tilted away from the nearest dolerite exposure. Although their orientation varies from place to place, there are two sets of fractures common in this rock unit. The dominant one i.e., with larger spacing, are oriented along 70^0 to 80^0 in north west direction and the less dominant one, with less spacing, are aligned 10^0 to 20^0 in north east direction.

According to Abdelwasie Hussein (2000), no primary porosity and permeability is seen in the thin section. This implies that the porosity and permeability of this rock unit is due to these intense fracturing.

3.2.3 The Shale-Limestone-Marl Intercalation Unit

This rock unit is mainly found on the southern and eastern parts of the study area (fig 3.1). About 2-meter thick shale and 0.5-meter thick limestone intercalation layers are exposed for about 20 meters on the hillsides of the southern margin of Aynalem valley. This intercalation layer is underlain by another marl-limestone-shale intercalation unit and overlain by 5 to 10 meter thick

sandstone bed. In most places the sandstone is tilted down the hill by 30 to 35 degree dip angle. On the southwestern part of the study area a sill of 5-meter thick dolerite exposure is observed underlain and overlain by the thinly bedded shale-limestone intercalation unit.

The unconsolidated shale is brown and dark gray in color. But the consolidated one, which is laminated, is gray when it is fresh and yellow when it is weathered.

The limestone is, light yellow when weathered, and gray when it is fresh, and observed mainly as boulders with the marl and forms a thin bed layer when it is together with the shale.

The marl is found as both consolidated and unconsolidated by forming lower slope on the hillside. It is yellow and sometimes dark in color. Mostly it is observed together with boulders of limestones.

The sandstone, which overlies to this rock unit, is white to yellow in color but some times it is also reddish.

Regionally, the Limestone and these rock units are correlated to the Antalo super sequence of Boselline et.al. (1997).

3.2.4 The Dolerite Rock Unit

This is found exposed as a network of sills and dykes almost in all parts of the study area. Most of the dykes form ridges and the sills are observed in the drilled log data. In almost all of the

wells the dominant rock type is dolerite. Mostly it is observed on the surface outcrop overlain by limestone and from the well log data it is also underlain by limestone (appendix-4).

It is black (fresh) and brown (weathered) in color and medium grained which contains phenocrysts of plagioclase crystals.

Exposures are highly affected by spheroidal weathering and fractured near the surface. Most of the fractures are aligned 40^0 to 60^0 in NW directions and in some places aligned $N10^0E$ and $N10^0W$.

According to Levitte (1970), from the thin section microscopic analysis, the rock consists of about 50% Plagioclase (Andesine), 40% Augite (Titanic), 2-5% Biotite, and 5% Opaque iron minerals.

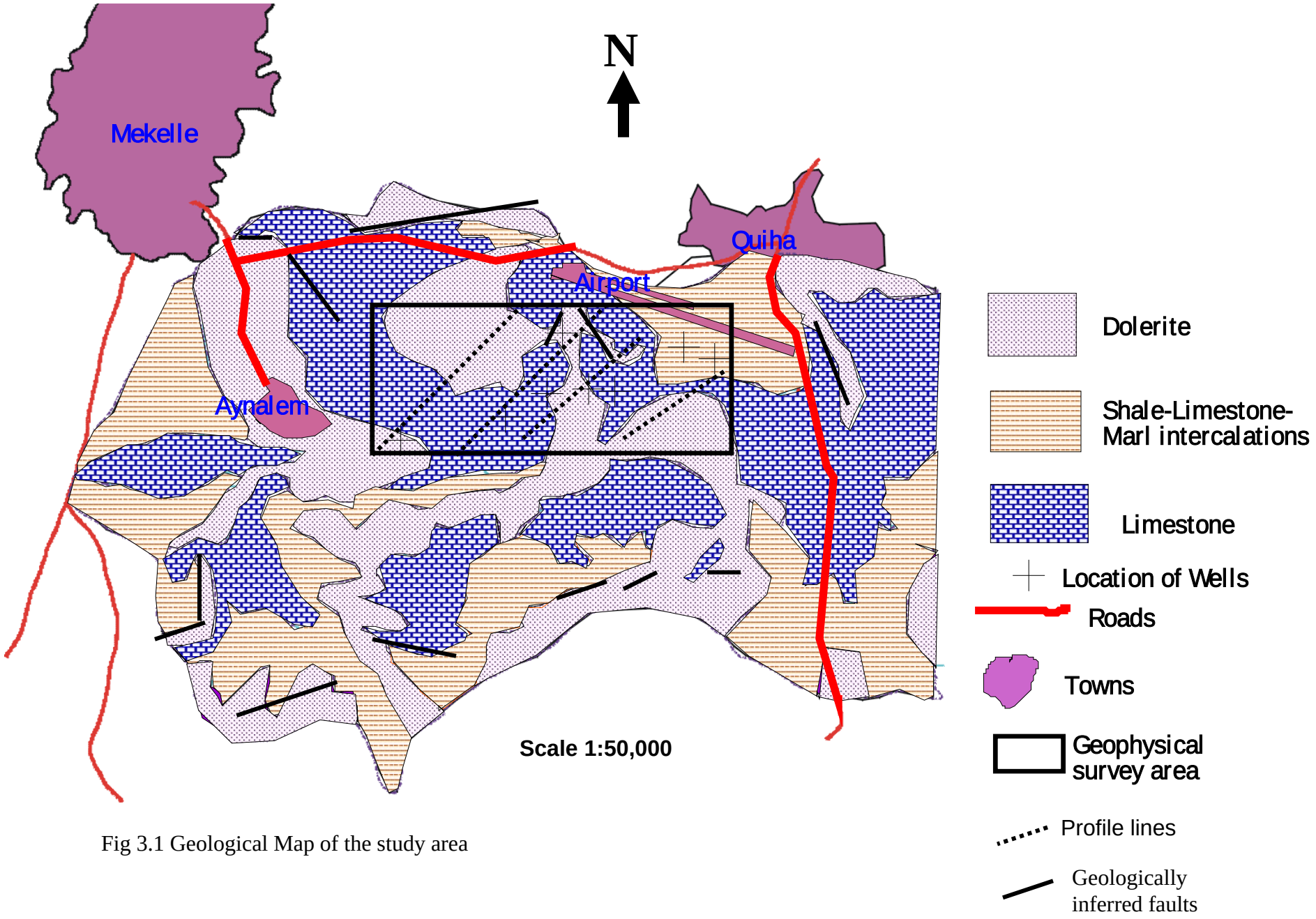

Fig 3.1 Geological Map of the study area

CHAPTER-4: GEOPHYSICS

4.1 Introduction

Refraction seismic, magnetic and electrical resistivity surveys were carried out along profiles shown in fig (4.1).

The fieldwork was conducted between February and March 2003 for about 50 days.

The purpose of the seismic refraction survey was to determine the type and thickness of the different layers, outline the water saturated zones and their thicknesses, to map the dolerite dykes and sills, and to detect faults or fractures and their orientations.

The magnetic survey was undertaken as a supplementary to the seismic investigation to detect structural trends such as fractures, lineaments, and geologic boundaries by measuring the variation of the earth's magnetic field intensity over the study area along the survey lines.

The electrical resistivty profiling was aimed mainly to delineate the water-saturated zones and detect vertical contacts so as to get an indication of lithologic differences. However, this is done only for one profile (fig 4.1) because of the instrumental failure.

The geologic result helps to select the appropriate profile directions for the geophysical surveys. From the surface observations most of the fractures are aligned along NW-SE directions.

Accordingly, the geophysical survey profiles are laid along NE-SW directions i.e., 55^0 North of East. And it also helps in the final interpretation of the geophysical survey.

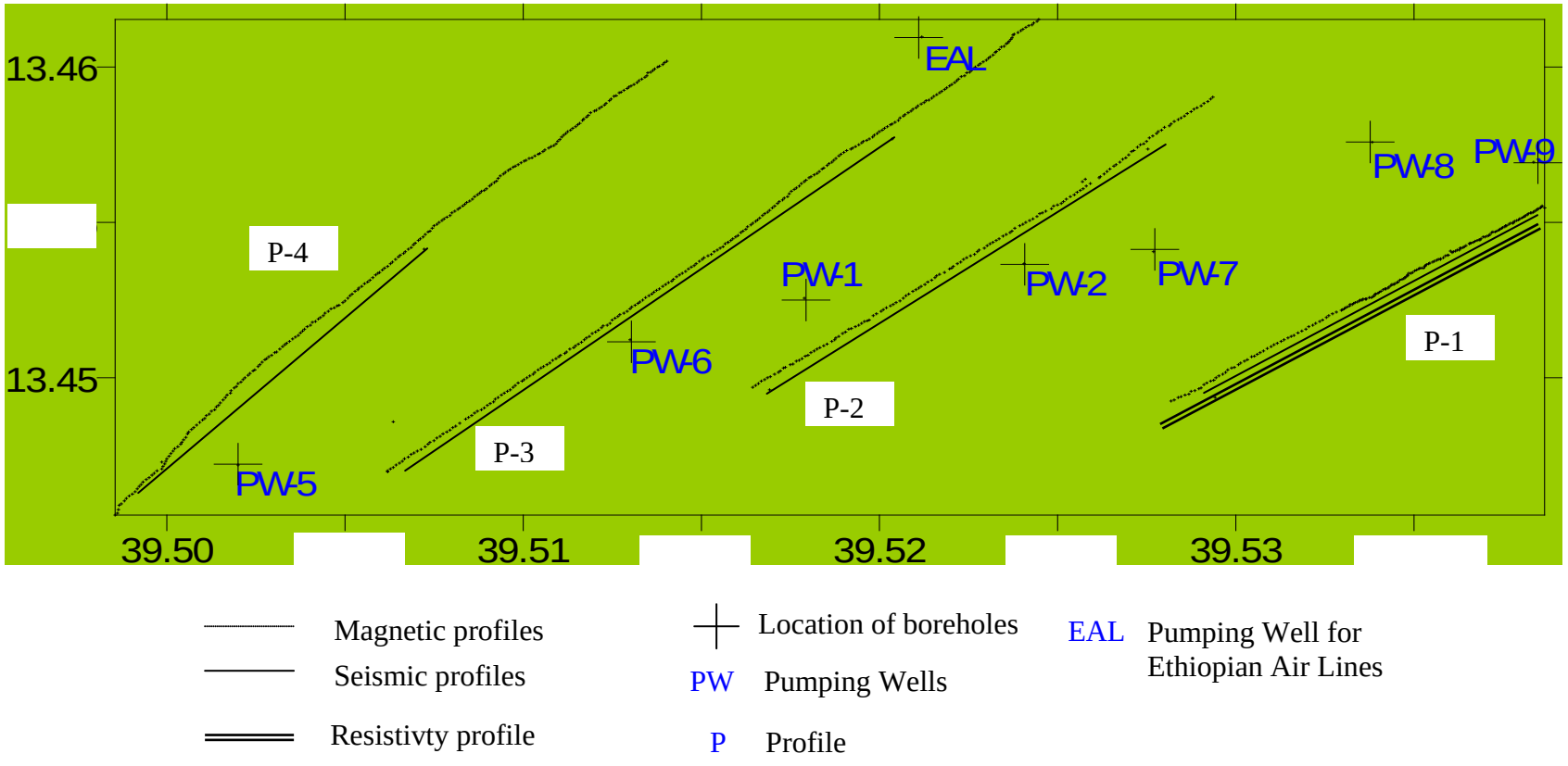

Fig 4.1 Geophysical survey lines and the location of eight boreholes.

4.2 Refraction Seismic Survey

4.2.1 Basic Theory and Principles of refraction seismic

4.2.1.1 Theory of elasticity and the wave equation

An object can be deformed in different ways by applying force on the sides of the object. Such application of force on the surface of an object is called stress. The stress deforms that object by changing its shape and size. Such deformation is called strain.

When the stressed rock masses are strained, energy is released and produces vibrations, which are called seismic waves.

Although there are different kinds of strain that can be produced depending on the strength and direction of stress and the nature of the substance being deformed, in seismic wave propagation the most interesting is the elastic strain. Because when the seismic waves travel away from the source, they produce only elastic strain.

This kind of strain is proportional to the applied stress, and it disappears when that stress ceases. A perfectly elastic body is the one that recovers completely after being deformed.

Solid substances ordinarily respond elastically to relatively weak, short-term stresses, and then exhibit plastic strain if stronger or more prolonged stress is applied.

For small magnitude, short duration stresses as in the case of seismic wave propagations, almost earth materials display a linear proportionality between stress and strain.

Hooke's law gives the most constitutive law for linear elasticity that relates stress to strain for homogeneous and isotropic medium. (Eq.1).

$$\tau_{ij} = C_{ijkl}\varepsilon_{kl} \quad \text{.....(1)}$$

Where τ_{ij} and ε_{kl} are elements of the stress and strain tensors respectively. C_{ijkl} is a third order tensor that relates the stress and strain tensor elements and it is called elastic moduli, which defines the elastic properties of the material. These properties are described in terms of Young's modulus, Poisson's ratio, Shear modulus, and the Bulk modulus. All these properties can be used to distinguish different solid substances.

By substituting $C_{ijkl} = \lambda\delta_{ij}\delta_{kl} + \mu\left(\delta_{ik}\delta_{jl} + \delta_{il}\delta_{jk}\right)$ and rearranging the kronecker delta functions, this form of Hooke's law for an isotropic linear elastic material is later formulated by Navier as

$$\tau_{ij} = \lambda\theta\delta_{ij} + 2\mu\varepsilon_{ij} \quad \text{.....(2)}$$

Where the strain is given as $\varepsilon_{ij} = \frac{\partial U_i}{\partial x_j}$ in terms of the displacement U and the dilatation θ, which is given as $\theta = \varepsilon_{ii} + \varepsilon_{jj} + \varepsilon_{kk}$. δ_{ij} is kronecker delta (e.g. $\delta_{kl}\varepsilon_{kl} = \varepsilon_{kk}$) and λ & μ are called Lame's constants.

The wave equation is derived from this stress-strain relation and from the homogeneous equation of motion.

$$\rho\frac{\partial^2 U_i}{\partial t^2} = \frac{\partial \tau_{ij}}{\partial x_j} \quad \text{.....(3)}$$

By equating the net force across a cube in terms of displacement and by replacing stress components with equivalent strain components in terms of displacement, the equation of motion can be written as:

$$\rho \frac{\partial^2 U_1}{\partial t^2} = (\lambda + \mu)\frac{\partial \theta}{\partial x_1} + \mu \nabla^2 U_1 \quad \text{……(4)}$$

$$\rho \frac{\partial^2 U_2}{\partial t^2} = (\lambda + \mu)\frac{\partial \theta}{\partial x_2} + \mu \nabla^2 U_2 \quad \text{……..(5)}$$

$$\rho \frac{\partial^2 U_3}{\partial t^2} = (\lambda + \mu)\frac{\partial \theta}{\partial x_3} + \mu \nabla^2 U_3 \quad \text{……..(6)}$$

Where U_1, U_2, & U_3 are displacements along x_1, x_2, and x_3 directions, ∇^2 is the Laplacian operator and ρ is density of the medium.

Adding equations 4, 5, & 6 and substituting the dilatation in terms of displacements

$$\theta = \nabla . \vec{U} = \frac{\partial U_1}{\partial x_1} + \frac{\partial U_2}{\partial x_2} + \frac{\partial U_3}{\partial x_3}$$

We get

$$\rho \frac{\partial^2 \vec{U}}{\partial t^2} = (\lambda + \mu)\nabla\left(\nabla . \vec{U}\right) + \mu \nabla^2 \vec{U} \quad \text{……..(7)}$$

Equation 7 is the three dimensional homogeneous equation of motion for a uniform, isotropic, linear elastic medium.

Using the vector identity

$$\nabla^2 \vec{U} = \nabla\left(\nabla . \vec{U}\right) - \nabla \times \nabla \times \vec{U}$$

Equation (7) can be written as

$$\rho \frac{\partial^2 \vec{U}}{\partial t^2} = (\lambda + 2\mu)\nabla\left(\nabla . \vec{U}\right) - \mu \nabla \times \nabla \times \vec{U} \quad \text{……(8)}$$

By making use of the following vector identities

$$\nabla.\left(\nabla\times\vec{U}\right)=\nabla\times\left(\nabla.\vec{U}\right)=0$$

For any vector U, we can derive the following two equations from equation (8) as follows.

$$\nabla.\rho\frac{\partial^2\vec{U}}{\partial t^2}=\nabla.((\lambda+2\mu)\nabla\left(\nabla.\vec{U}\right)-\mu\nabla\times\nabla\times\vec{U})$$

$$\rho\frac{\partial^2\nabla.\vec{U}}{\partial t^2}=(\lambda+2\mu)\nabla^2\left(\nabla.\vec{U}\right)\qquad\text{Replacing}\quad\nabla.\vec{U}=\theta$$

$$\rho\frac{\partial^2\theta}{\partial t^2}=(\lambda+2\mu)\nabla^2\theta\qquad\text{Or}\quad\frac{1}{\alpha^2}\frac{\partial^2\theta}{\partial t^2}=\nabla^2\theta\ \ldots\ldots\ldots\ldots\ldots\ldots(9)$$

Where $\alpha^2=\dfrac{\lambda+2\mu}{\rho}$ and α is the velocity (speed) of the compression or p-waves.

So equation (9) is a wave equation that relates the displacement and elastic constants of the material of compression waves.

Similarly the shear wave equation can be also obtained from equation (8) as:

$$\rho\frac{\partial^2\left(\nabla\times\vec{U}\right)}{\partial t^2}=\nabla\times\nabla\left(\nabla.\vec{U}\right)-\mu\nabla\times\nabla\times\left(\nabla\times\vec{U}\right)$$

$$\rho\frac{\partial^2\omega}{\partial t^2}=-\mu\nabla\times\nabla\times\omega\ \ldots\ldots\ldots\ldots\ldots\ldots\ldots\ldots\ldots\ldots\ldots\ldots\ldots\ldots\ldots\ldots\ldots\ldots\ldots(10)$$

Where ω is called the rotation which is an essential feature of S-waves and given as $\omega=\nabla\times\vec{U}$.

By the vector identity, $\nabla^2\omega=\nabla\left(\nabla.\omega\right)-\nabla\times\nabla\times\omega=-\nabla\times\nabla\times\omega$, equation (10) can be written as

$$\rho\frac{\partial^2\omega}{\partial t^2}=\mu\nabla^2\omega\ \ldots\ldots\ldots\ldots\ldots\ldots\ldots\ldots\ldots\ldots\ldots\ldots\ldots\ldots\ldots\ldots\ldots\ldots\ldots\ldots\ldots\ldots..(11)$$

Equation (11) is called the shear wave equation and its phase speed β is given as

$$\beta^2 = \frac{\mu}{\rho}.$$

So the seismic waves, which are composed of the compression and shear waves, are propagating in the earth materials at different velocities depending on the elastic properties of that material. That means different rock layers can be identified based on the different velocities of the seismic waves that propagate through these rocks.

4.2.1.2 The Basic Principles of Refraction Seismic

The refraction seismic is an output of three basic principles and the methods of trigonometry and geometry. These are the applications of Snell's law, Fermat's and Huygens principles.

Snell's law: says "the directions of refracted and reflected waves traveling away from a boundary depend on the direction of the incident wave and the speeds of the waves. Look at the following equation (12) and figure (4.2) below.

$\text{Sin } i/\text{Sin } r = V_1/V_2$ ……(12)

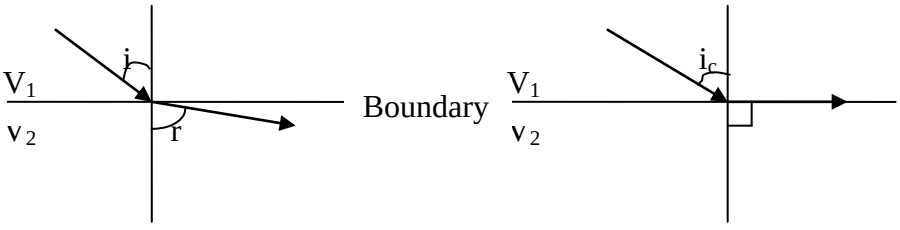

Fig. 4.2 Refracted waves along a boundary.

Equation (12) is called Snell's law where i and r are the angles of incident and refracted rays respectively. V_1 and V_2 are speeds of the incident and refracted rays inside the two layers.

At critical refraction (when angle $r=90^0$ and i=ic), the refracted wave is produced by an incident wave traveling along the ray that reaches the boundary at the critical angle of incidence ic. For this case of critical refraction, sin r=sin 90=1, the Snell's law can be written as

$$\text{Sin } i_c = V_1/V_2 \ldots\ldots\ldots\ldots\ldots\ldots\ldots\ldots\ldots\ldots\ldots\ldots\ldots\ldots\ldots\ldots\ldots(13)$$

Which shows how the critical angle depends on the wave speeds.

There are three consequences of Snell's law;

1) If the velocity of the two layers V_1 and V_2 are equal, the two angles i and r are equal and there will be no refraction.
2) If V_1 is greater than V_2, angle i will be greater than r and as a result the refracted wave always goes down. It doesn't go up. This is the main problem of seismic refraction method for rock layers with low velocity at depths. And this problem is called velocity reversal problem.
3) This third consequence is very important for the seismic refraction method. When V_1 less than V_2 i.e., when the velocity increases towards depth, r will be greater than i as a result there will be a refracted wave from the depth to the surface and then recorded by Seismometers (geophones).

Fermat's principle: says "elastic waves travel between two points along paths requiring the least time. Its mathematical meaning is as shown below.

Consider a wave traveling from source S through a two layer formation with velocity V_1 and V_2 crossing the interface at A to the second layer up to G. (fig 4.3)

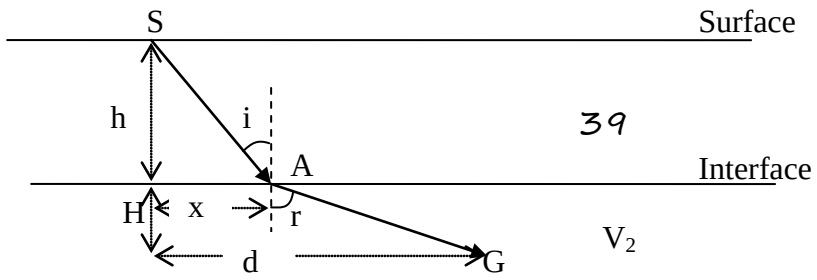

Fig 4.3 Wave propagation in two layer formations

$$SA = \frac{x}{\sin i} = \sqrt{h^2 + x^2} \qquad \text{and} \qquad AG = \frac{d-x}{\sin r} = \sqrt{H^2 + (d-x)^2}$$

The total time t taken for the ray along the path SG is:

$$t = SA/V_1 + AG/V_2 = \frac{1}{V_1 V_2}\left[V_2\sqrt{h^2 + x^2} + V1\sqrt{H^2 + (d-x)^2}\right] \ldots\ldots\ldots\ldots\ldots\ldots (14)$$

For the time t to be minimum, we must differentiate equation (14) with respect to distance (x) and equating to zero.

That is $\frac{dt}{dx} = 0$ and gives

$$V_2 \frac{x}{\sqrt{x^2 + h^2}} = V_1 \frac{d-x}{\sqrt{H^2 + (d-x)^2}} \qquad \text{Or} \qquad V_2 \text{ Sin i} = V_1 \text{ Sin r} \ldots\ldots\ldots\ldots\ldots\ldots (15)$$

The Fermat's principle leads to Snell's law. This implies that the particular path requiring the least time is the path predicted from Snell's law.

Huygen's principle: waves in a homogeneous medium spread out from a point source as expanding spheres. Huygen's principle states "every point on a wave front is the source of a new wave that also travels out from it in spherical shells.

If the spherical waves have a large enough radius, they can be treated as planes.

Lines perpendicular to the wave fronts, called wave paths or rays, can often be used to describe the wave propagation more conveniently than wave fronts.

4.2.2 Geometry of Refracted waves

4.2.2.1 The Single Layer Refraction

When the seismic waves reach a boundary between two substances or rock layers in which the

wave speeds are different, they divide into waves that bounce, or reflect, from the boundary and other waves that pass, or refract, across the boundary.

For simplicity let's consider a single refractor with two homogeneous layers. The travel time curve becomes two linear segments with different slopes as shown in fig (4.4).

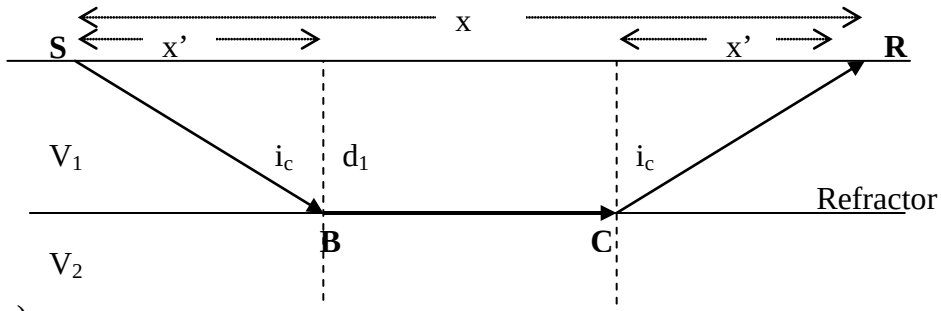

a)

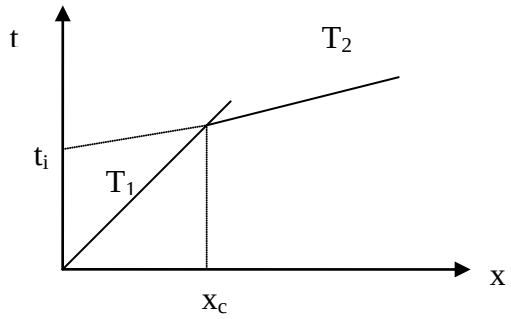

b)

Fig 4.4 Travel-time of direct & refracted waves from a shot point in two-layer system (a) and their travel time curves (b).

The first line in fig 4.4 (b) represents the arrival of direct waves and the second one is for the refracted waves.

The time taken for the direct wave to reach the receiver R from the source S in fig 4.4 (a) is given as

$T_1 = X/V_1$ …… (16)

And for the refracted wave

$T_2 = SB/V_1 + BC/V_2 + CR/V_1$ ……(17)

SB = SR = d1/cos i_c x' = d1 tan i_c and BC = x-2x' = x- 2d1 tan i_c

Thus equation (17) can be rewritten as

$$T_2 = \frac{2d_1}{V_1} + \frac{x - 2d_1 \tan i_c}{V_2}$$

Using Snell's law it becomes

$$T_2 = \frac{2d_1}{V_1 \cos i_c}\left(1 - \sin^2 i_c\right) + \frac{x}{V_2}$$

Then substituting $\cos i_c = \sqrt{1 - \sin^2 i_c}$ and $\sin^2 i_c = \frac{V_1^{\,2}}{V_2^{\,2}}$, finally

$$T_2 = \frac{2d_1}{V_1 V_2}\sqrt{V_2^{\,2} - V_1^{\,2}} + \frac{x}{V2} \quad \text{……..(18)}$$

The gradients of the two travel time curves (T1 and T2) can be obtained by differentiating equations (16) and (18) respectively as follows.

$$\frac{dT_1}{dx} = \frac{1}{V_1} \qquad \text{And} \qquad \frac{dT_2}{dx} = \frac{1}{V_2}$$

This implies that the velocity of the two layers V_1 and V_2 can be obtained from the slopes of the travel time curves.

There are two ways of obtaining the depth (d_1) to the refractor. Intercept time method and crossover distance methods.

Intercept time (t_i) method:

The intercept time t_i is the point at which the straight line representing the refracted waves intersects the vertical axis of the travel time graph. (Fig 4.4 (b)).

Recalling equation (18), at $T_2 = t_i$, x is zero, thus

$t_i = \frac{2d_1}{V_1 V_2}\sqrt{V_2^{\,2} - V_1^{\,2}}$ And from this

$$d_1 = \frac{t_i V_1 V_2}{2\sqrt{V_2^{\,2} - V_1^{\,2}}} \quad \text{.....(19)}$$

The crossover distance method:

In the travel time curve (fig 4.4; b), the distance at which the two straight lines intersect is called the crossing distance $x_{c.}$ A geophone placed at this distance would receive both the direct wave and the refracted wave at exactly the same time. For all distances beyond x_c, the refracted wave will be the first arrival, and the direct wave will become a later arrival and before the x_c direct waves arrived first.

Suppose that a source S and a receiver R are separated by the distance x, as shown in figure 4.4 (a).

And the travel time equations both for the direct and refracted waves are given in equations (16) and (18) respectively.

At the crossing distance $x = x_c$, we can set equation (16) equal to equation (18) to obtain

$$\frac{x_c}{V_1} = \frac{x_c}{V_2} + \frac{2d_1}{V_1 V_2}\sqrt{V_2^{\,2} - V_1^{\,2}}$$

By rearranging to solve for d_1 finally we get

$$d_1 = \frac{x_c}{2}\sqrt{\frac{V_2 - V_1}{V_2 + V_1}} \quad \text{..... (20)}$$

Equations (19) and (20) are equally important. To summarize, after the travel time curve has been prepared, the velocities v_1 and v_2 can be obtained from the slopes of the two straight lines. Then

the intercept time t_i and the crossing distance x_c can be observed from the travel time curves. All these values are used to calculate the layer thickness.

4.2.2.2 Refracted Waves In Multi Layered Structures

To analyze refracted seismic waves in a multi layered structure we can use the same method that we have introduced for a single layer. First let's consider a three layer case.

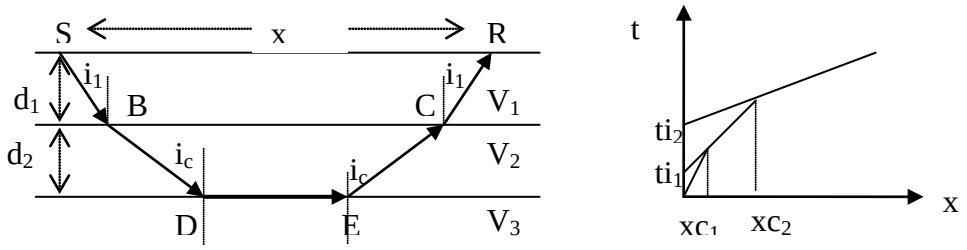

a) b)

Fig 4.5 Travel time of direct and refracted waves in a three-layer case (a) & their travel time curves (b).

From Snell's law

$$\frac{\sin i_1}{V_1} = \frac{\sin i_c}{V_2} = \frac{1}{V_3}$$

Similarly the total travel time for the ray refracted from the third layer is

$$T_3 = \frac{SB + RC}{V_1} + \frac{BD + CE}{V_2} + \frac{DE}{V_3} = \frac{2d_1}{V_1}\cos i_1 + \frac{2d_2}{V_2}\cos i_c + \frac{x}{V_3} \quad \text{.....(21)}$$

For four layers

$$T_4 = \frac{2d_1}{V_1}\cos i_1 + \frac{2d_2}{V_2}\cos i_2 + \frac{2d3}{V_3}\cos i_c + \frac{x}{V_4} \quad \text{.....(22)}$$

Therefore, for n horizontal layers with thickness d_1, d_2… d_{n-1} and wave velocities V_1, V_2… Vn, the travel time equation will be

$$T_n = \frac{x}{V_n} + 2\sum_{j=1}^{n-1} \frac{d_j}{V_j} \cos i_j \quad \text{Or} \quad T_n = \frac{x}{V_n} + 2\sum_{j=1}^{n-1} \frac{d_j}{V_j V_n} \left(V_n^{\,2} - V_j^{\,2}\right)^{1/2} \quad \text{……(23)}$$

T_n is the time taken for the ray that critically refracted along the top surface of the n^{th} layer.

The intercept time determined from waves reaching the deepest refractor will be

$$ti_n = 2\sum_{j=1}^{n-1} \frac{d_j}{V_j} \cos i_j \quad \text{……(24)}$$

And the depth of the deepest layer will be

$$dn = \left(\frac{ti_n}{2} - \sum_{j=1}^{n-1} \frac{d_j}{V_j} \cos i_j \right) \frac{V_n}{\cos i_n} \quad \text{……(25)}$$

4.2.2.3 Refraction seismic in the case of dipping layers

In horizontal layers the down going and up going parts of a refracted ray path are similar. This is not true for waves that are critically refracted in a structure possessing dipping layers. If the rock layers are dipping, seismic waves follow complicated paths.

In this case the true refractor velocities can not be determined by firing a shot at only one end of a seismic line (spread), but such velocities can be determined if arrival times are recorded from both ends.

Consider the following fig. with dipping subsurface layer.

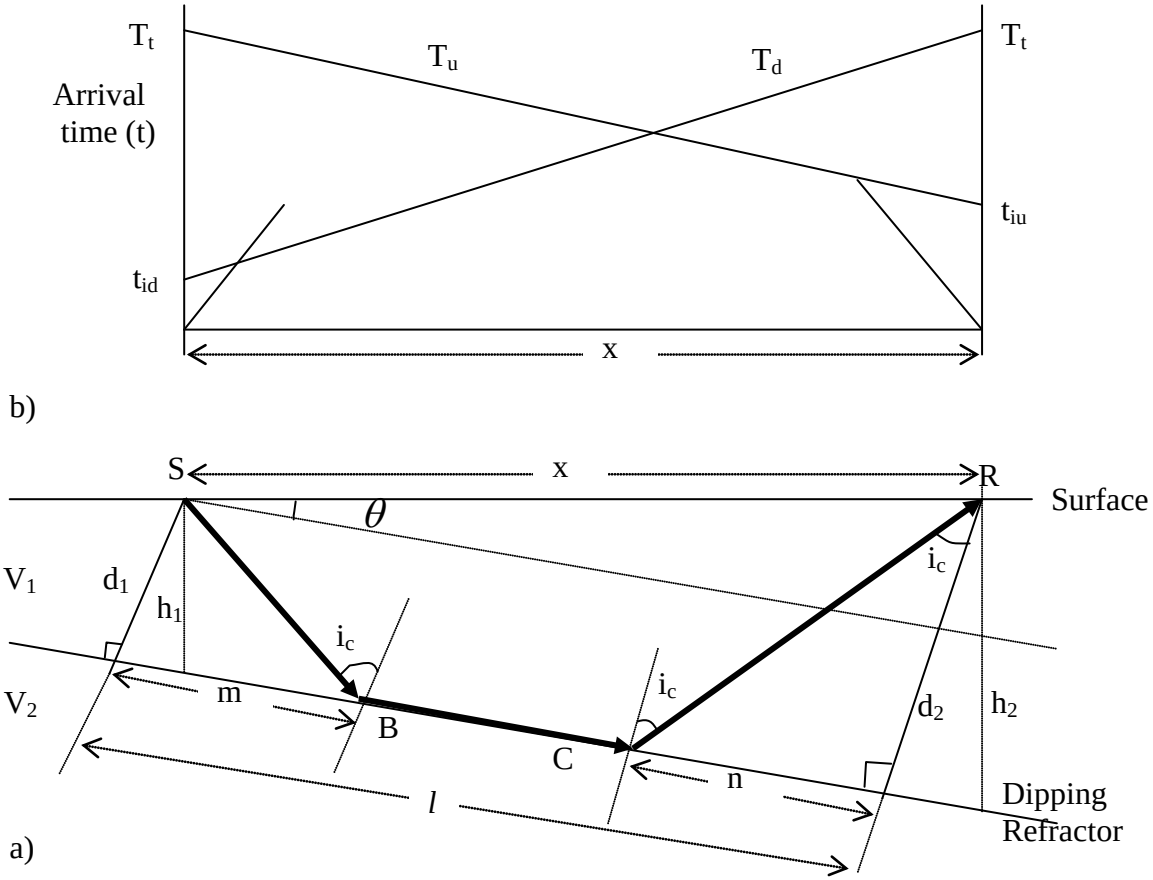

Fig 4.6 Refraction in the case of dipping layers (a) and the travel time curves of both forward and reveres shots (b).

So the total travel time for the down going refracted wave (Td) taken from the source to the receiver at a horizontal distance x is;

$$T_d = \frac{SB}{V_1} + \frac{BC}{V_2} + \frac{CR}{V_1} \quad \text{……..(26)}$$

$$SB = \frac{d_1}{\cos i_c}, \quad CR = \frac{d_2}{\cos i_c} \quad \textit{and}$$

$$BC = l - m - n = l - d_1 \tan i_c - d_2 \tan i_c$$

$$T_d = \frac{d_1}{V_1 \cos i_c} + \frac{d_2}{V_1 \cos i_c} + \frac{l}{V_2} - \frac{d_1 \tan i_c}{V_2} - \frac{d_2 \tan i_c}{V_2}$$

Using Snell's law $V_2 = \frac{V_1}{\sin i_c}$

$$T_d = \frac{d_1 \cos i_c + d_2 \cos i_c}{V_1} + \frac{l}{V_2}$$

Substituting $l = x\cos\theta \quad \textit{and} \quad d_2 = d_1 + x\sin\theta$

$$T_d = \frac{2h_1 \cos i_c + x \sin\theta \cos i_c}{V_1} + \frac{x\cos\theta}{V_2}$$

Replace $V_2 = \frac{V_1}{\sin i_c}$ and $\sin\theta\cos i_c + \cos\theta \sin i_c = \sin(i_c + \theta)$

Finally it becomes

$$T_d = \frac{2d_1 \cos i_c + x \sin(i_c + \theta)}{V_1} \quad \text{.....(27)}$$

If there is another source on the other end at R on the above figure 4.6 (a), the wave propagates upward to S on the same path but with different velocity.

Similarly the total travel time for the up going refracted wave (T_u) is:

$$T_u = \frac{d_1}{V_1 \cos i_c} + \frac{d_2}{V_1 \cos i_c} + \frac{l}{V_2} - \frac{d_1 \tan i_c}{V_2} - \frac{d_2 \tan i_c}{V_2}$$

Substituting $d_1 = d_2 - x \sin\theta$

Finally it becomes

$$T_u = \frac{2d_2 \cos i_c + x \sin(i_c - \theta)}{V_1} \quad \text{.....(28)}$$

Differentiating equations (27) and (28) with respect to x to calculate the gradient of the travel time curves

$$\frac{dT_d}{dx} = \frac{\sin(i_c + \theta)}{V_1} = \frac{1}{V_{2d}} \quad \text{and} \quad \frac{dT_u}{dx} = \frac{\sin(i_c - \theta)}{V_1} = \frac{1}{V_{2u}} \quad \text{.....(29)}$$

Recalling equation (18) for non-dipping horizontal interfaces, the gradient

$$\frac{dT_2}{dx} = \frac{1}{V_2} = \frac{\sin i_c}{V_1}$$

From these the true velocities V_2 for the refractor of dipping down, dipping up, and non-dipping horizontal interfaces are given as follows respectively.

$$V_{2d} = \frac{V_1}{\sin(i_c + \theta)}$$

$$V_{2u} = \frac{V_1}{\sin(i_c - \theta)}$$

$$V_2 = \frac{V_1}{\sin i_c}$$

This implies that the velocities of the waves depend on the dipping angle θ and as a result from the above equations the value of the true velocity V_2 is between V_{2d} and V_{2u} for the same refractor with dipping angle θ.

$$\frac{1}{V_{2d}} = \frac{\sin(i_c + \theta)}{V_1} \Rightarrow i_c + \theta = \sin^{-1}\left(\frac{V_1}{V_{2d}}\right) \text{.....(30)}$$

$$\frac{1}{V_{2u}} = \frac{\sin(i_c - \theta)}{V_1} \Rightarrow i_c - \theta = \sin^{-1}\left(\frac{V_1}{V_{2u}}\right) \text{.....(31)}$$

From equations (30) and (31), we can formulate ic and θ as follows.

$$i_c = \frac{1}{2}\left\{\sin^{-1}\left(\frac{V_1}{V_{2d}}\right) + \sin^{-1}\left(\frac{V_1}{V_{2u}}\right)\right\} \text{.....(32)}$$

$$\theta = \frac{1}{2}\left\{\sin^{-1}\left(\frac{V_1}{V_{2d}}\right) - \sin^{-1}\left(\frac{V_1}{V_{2u}}\right)\right\} \quad \text{……..(33)}$$

By the time intercept method the depth d_1 and d_2 are given as

$$d_1 = \frac{V_1 t_{id}}{2\cos i_c} \quad \text{and} \quad d_2 = \frac{V_1 t_{iu}}{2\cos i_c} \quad \text{……..(34)}$$

But the true vertical depth h_1 and h_2 beneath each shots at both ends depend on the dipping angle θ as follows.

$$h_1 = \frac{d_1}{\cos\theta} = \frac{V_1 t_{id}}{2\cos i_c \cos\theta} \quad \text{and} \quad h_2 = \frac{d_2}{\cos\theta} = \frac{V_1 t_{iu}}{2\cos i_c \cos\theta} \quad \text{……..(35)}$$

The reversed profile (shooting from both sides), offers a significant advantage in that the true velocities and thickness of layers can be computed.

Using sources on both ends of the spread, first we determine V_1, V_{2d} and V_{2u} from the gradients of the travel time curves in fig 4.6 (b). After that we can calculate the critical angle i_c and the dipping angle θ of the refractor by using equations (32) and (33). Then we determine the true depths beneath each shots. The depth computed from an intercept time represents the depth of the refracting surface project back to the shot point.

As shown in figure 4.6(a) d_1 and d_2 are perpendicular depths to the interface and h_1 and h_2 are the vertical true depths of the interface from the surface just beneath the source S and the receiver R respectively.

Depths beneath each geophone can be determined by means of Generalized Reciprocal Method (GRM) and the Delay Time methods to allow mapping of irregular boundaries (refractors).

4.2.3 Refraction Seismic Interpretation Techniques

4.2.3.1 The Delay Time Method

This method is explained as follows. The delay in time is the difference between the time actually spent by the wave traveling on its downward or upward path through the upper layer, and the time it would have spent traveling at the refractor velocity along the normal projection of this path on the interface (Redpath, 1973).

That is, the delay time from shot one (S1) to the geophone (G) in figure 4.7 (a) is

$$\Delta T_1 = \frac{S_1 A}{V_1} + \frac{AB}{V_2} + \frac{BG}{V_1} - \frac{S_1'G'}{V_2} = T_{t1} - \frac{S_1'G'}{V_2} \quad \text{.....(36)}$$

And similarly from S2 to the geophone G is

$$\Delta T_2 = \frac{S_2 D}{V_1} + \frac{CD}{V_2} + \frac{CG}{V_1} - \frac{G'S_2'}{V_2} = T_{t2} - \frac{G'S_2'}{V_2} \quad \text{.....(37)}$$

b)

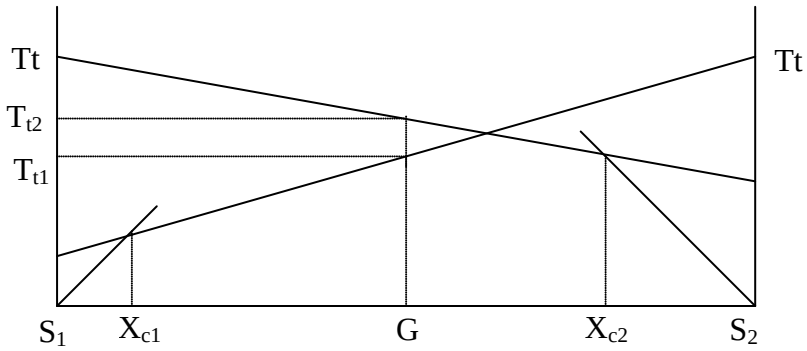

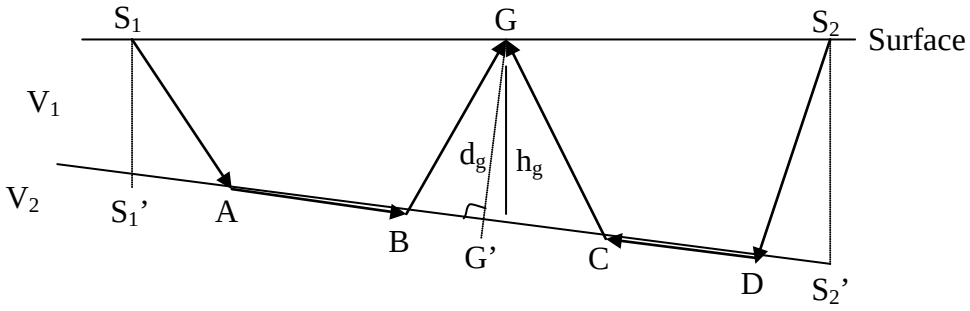

a)

Fig 4.7 refracted waves from both the forward and reveres shots leaving the refractor at different points and arrive at the same geophone (a) and their travel time curves (b).

And similarly the total delay time from S_1 to a geophone at S_2 can be formulated as

$$\Delta T = \frac{S_1 A}{V_1} + \frac{AD}{V_2} + \frac{DS_2}{V_1} - \frac{S_1'S_2'}{V_2} = Tt - \frac{S_1'S_2'}{V_2} \quad \text{.....(38)}$$

And by adding equations (36) & (37), the total delay time becomes;

$$\Delta T = T_{t1} + T_{t2} - \left(\frac{S_1'G' + S_2'G'}{V_2} \right) = T_{t1} + T_{t2} - \frac{S_1'S_2'}{V_2} \quad \text{.....(39)}$$

Thus from equations (38) & (39),

$$\Delta T = \frac{1}{2}\left[T_{t1} + T_{t2} - Tt\right] \text{ ……..(40)}$$

Where ΔT the delay time, Tt is the reciprocal time, T_{t1} and T_{t2} are the arrival times from shot-1 and shot-2 at the same geophone G.

From fig.4.7 (a),

$$\Delta Tg = \frac{BG}{V_1} - \frac{BG'}{V_2} = \frac{d_g}{V_1 \cos i_c} - \frac{d_g \tan i_c}{V_2} \text{ ……..(41)}$$

From this,

$$d_g = \frac{\Delta Tg V_1}{\cos i_c} = \frac{\Delta Tg V_1}{\cos\left(\sin^{-1}\frac{V_1}{V_2}\right)} \text{ ……(42)}$$

But the true depth beneath the geophone G is given as;

$$h_g = \frac{d_g}{\cos\theta} = \frac{1}{\cos\theta}\frac{\Delta Tg V_1}{\cos\left(\sin^{-1}\frac{V_1}{V_2}\right)} \text{ ……(43)}$$

Where θ is the dip angle of the refractor, ΔTg is the delay time for that geophone, d_g is the depth perpendicular to the refractor and h_g is the true depth of the refractor exactly beneath that geophone, which is perpendicular to the surface.

It is important to note that the method of delay time can be applied only when there is overlap between arrivals refracted from the same layer. In the case of the two shots S_1 and S_2 in Fig 4.7, this method works only for the geophones between x_{c1} and $x_{c2.}$

But for the rest of the geophones out of x_{c1} and x_{c2}, we need to extrapolate the first set of refracted arrivals back towards the shot point by using arrival times from additional shots beyond-the-end shots. Both of the arrivals from the end shot and beyond-the-end shots must be refracted from the same interface. This technique is called phantoming. If the plot of arrival times from the beyond-the-end shot parallels that of the end shot, they represent refractions from the same layer.

Therefore, more than four shots are required on both sides of the spread to allow delay times to be determined over the entire spread so as to compute the depth to the refractor beneath every geophone.

4.2.3.2 The Generalized Reciprocal Method (GRM)

According to Palmer (1980), the GRM is a powerful method of seismic refraction interpretation well suited to irregular refractor configuration and lateral changes in refractor velocity.

This method uses a pair of geophone positions on the surface where the forward and reverse rays leaving the refractor at the same point arrive at the geophone positions, such as X and Y (fig 4.8).

The travel times at two geophones, separated by the variable distance XY, are used in refractor velocity analysis and time depth calculations (equations 44 & 47)**.** This results in the refractor velocity analysis being the simplest and the time depths showing the most detail.

But in the case of time delay method in fig 4.7 (a) the XY value is zero and this makes the irregular refractor topography interpreted as smooth.

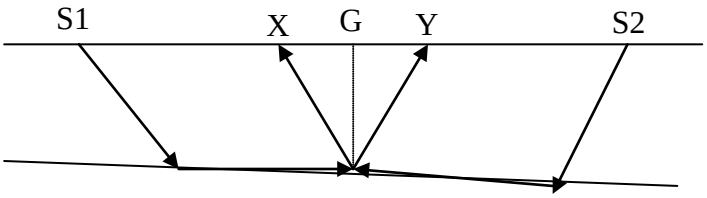

Fig 4.8 Paths of forward and reveres refracted waves leaving the refractor at the same point and arrive at different geophones.

Using the symbols of the above figure, the velocity analysis function, t_v, used in GRM interpretation is determined through the following equation.

$$t_v = \frac{1}{2}\left(t_{s1y} - t_{s2x} + t_{s1s2}\right) \quad \text{.....(44)}$$

The value of this function is referred to G, which is midway between X and Y.

Values of t_v calculated using the above equation are plotted against distance for different XY values. The proper curve to use in determining the refractor velocities is the one that exhibits the least amount of irregularity. The XY value which gives the simplest curve is the one at which the forward and the reverse rays emerge from nearly a common point on the refractor and it is called the optimum XY value.

The inverse of an apparent refractor velocity V'_n is defined as the slope of a line fitted to the t_v values for the optimum XY. I.e.,

$$\frac{dt_v}{dx} = \frac{1}{V'_n} \quad \text{.....(45)}$$

It can be shown (Palmer, 1980) that

$$V_n = V'_n \cos\theta_{n-1} \quad \text{.....(46)}$$

Where V_n is the true refractor velocity and θ_{n-1} is the dip angle of the refractor.

The generalized time-depth at G is defined by the equation

$$t_G = \frac{1}{2}\left[t_{S1Y} + t_{S2X} - \left(t_{S1S2} + \frac{XY}{V'_n} \right) \right] \quad \text{.....(47)}$$

The curve that defines the optimum XY is the one that shows the maximum amount of detail, i.e., the most irregular curve. This is opposite to the least irregular criterion used in the velocity analysis.

The time depth t_G is not the true depth of the refractor but it shows the shape of the refracting horizon in time.

Recalling fig 4.7 (a), the time depth for the delay time method is;

$$t_G = \frac{1}{2}\left[t_{S1G} + t_{S2G} - t_{S1S2} \right] = \Delta Tg \quad \text{.....(48)}$$

In this case t_G is actually the delay time and no knowledge of the refractor velocity is required for the calculation of the time depth unlike that of the GRM.

The generalized time-depth function t_G is related to the thickness and velocities of each layer overlying the target refractor at each geophone position through the following equation.

$$t_G = \sum_{j=1}^{n-1} Z_{jG} \frac{\left(V_n^{\,2} - V_j^{\,2}\right)^{1/2}}{V_j V_n} \quad \text{……..(49)}$$

Once the optimum XY distance for a target refractor is known, an average velocity from the surface to the refractor can be determined regardless of whether or not all overlying layer thicknesses and velocities are known using the following equations.

$$\overline{V} = \left[\frac{V' XY}{XY + 2t_G V'}\right]^{1/2} \quad \text{……(50)}$$

$$Z = \frac{t_G \overline{V}}{\cos i} \quad \text{……(51)}$$

Where $i = \sin^{-1}\left(\frac{\overline{V}}{V'}\right)$, $\overline{V}$ and V' are the average and the refractor's velocities, and Z is the depth to the target refractor.

4.2.4 Data Acquisition, Processing, and Interpretation

4.2.4.1 Instrumentation

The survey was conducted using a Japan-OYO made 24-channel digital seismograph McSEIS-SX. This 8-kg instrument has a 12 VDC battery for the power supply. All the data collected is stored on the hard disk, which is able to store up to 250 MB (i.e. about 512 data files). And it has a floppy disk and zip drives.

An 8-kg sledgehammer was used to generate the seismic waves. Hammering was made on an iron plate.

4.2.4.2 Data acquisition

The aim of the refraction seismic field survey was to measure the speed of a seismic wave along different parts of its path in the rock formations. Every wave reaching the geophone produces a momentary impulse on a record of ground vibration called seismogram (fig 4.9).

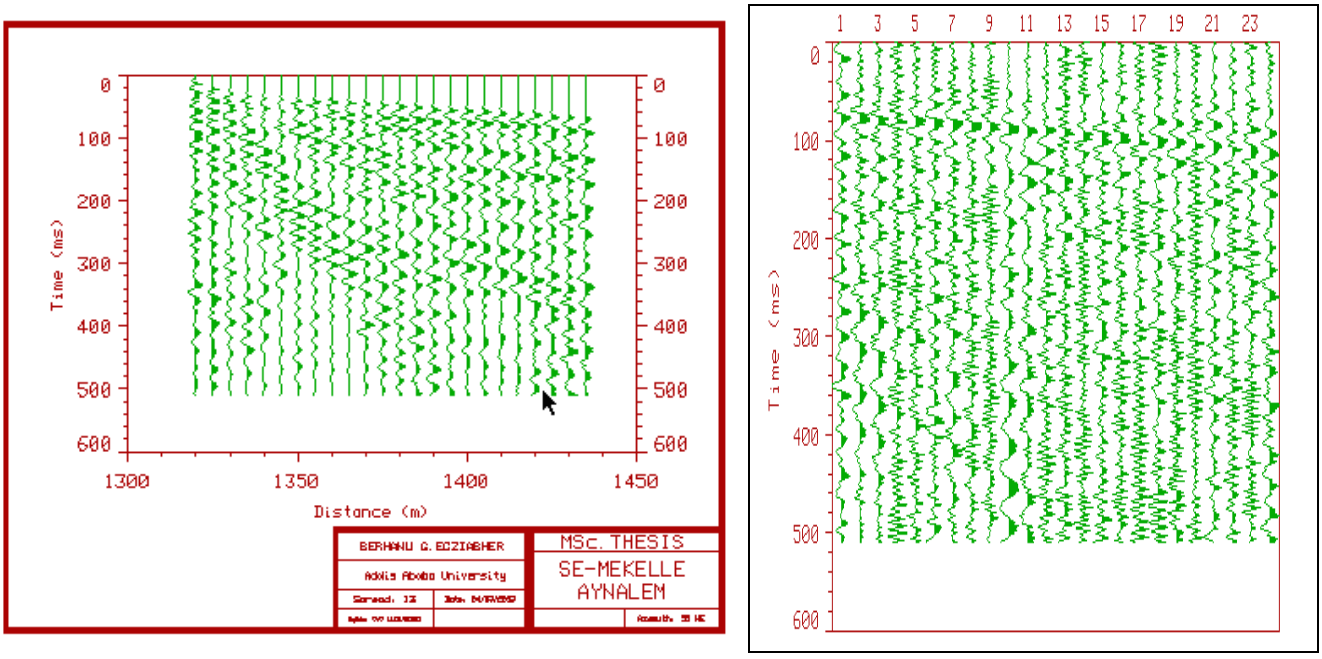

a) b)

Fig 4.9 Examples of recorded seismic data (a) pure and (b) noisy data.

The data collection was performed by placing 24 geophones with 5m spacing along a straight line, which covers 115m(one spread). Seven shots were made per spread. The distances between each shots are shown in the figure below.

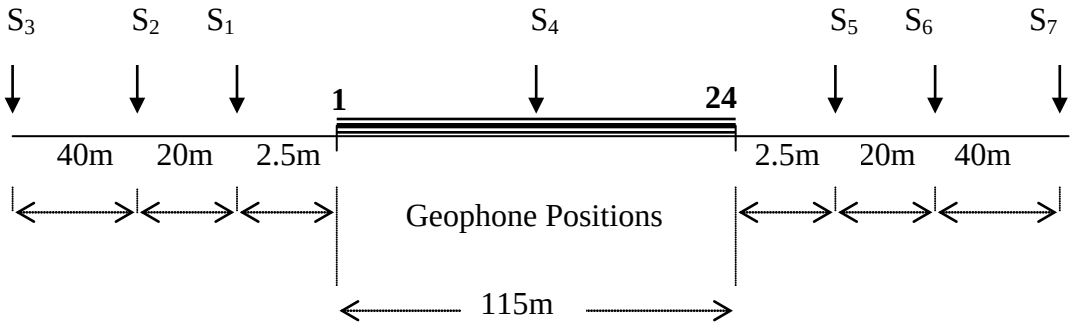

Fig 4.10 The geophone and shot-point positions of a spread.

There was an overlap of two geophones between each spreads. That is, the 23rd and 24th geophone positions on the first spread were replaced by the 1st and 2nd geophones on the next spread.

In this survey seismic data were collected along a total of 51 spreads from 357 shot points, which cover about 5.87 km along four survey lines (fig 4.1).

The serious difficulty during this survey was the unwanted vibrations (noises) caused by wind (see fig 4.9, b). To minimize the effect of the wind the geophones were somewhat buried deep into the ground and the record was made by stacking up to 30 times for each source.

4.2.4.3 Data processing and presentation

The first step of the seismic refraction data processing was picking the first arrival times from the seismograms (fig 4.11).

First arrival times were picked using the commercial software FIRSTPIX $^{TM}_{V\ 4.0}$ (Interpex ltd).

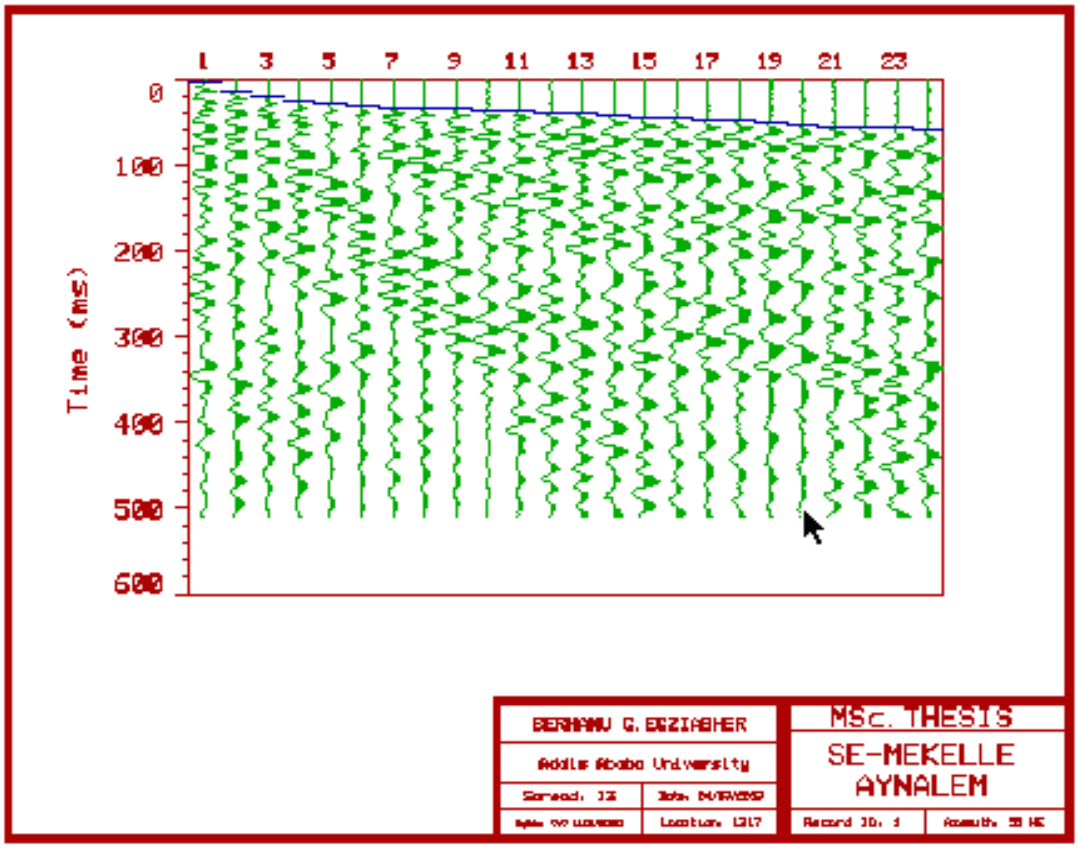

Fig 4.11 A sample of picked first arrivals on a seismogram.

After picking the first breaks on all records in a spread, the travel time (time-distance) curves were created for each shots in the spread as shown in figure 4.12. These curves are the first arrival times versus the shot-geophone distances.

Parallelism between the alignments of points on the time distance curve, corresponding to velocities of seismic waves through the same rock layers, were examined to find the likely number of layers.

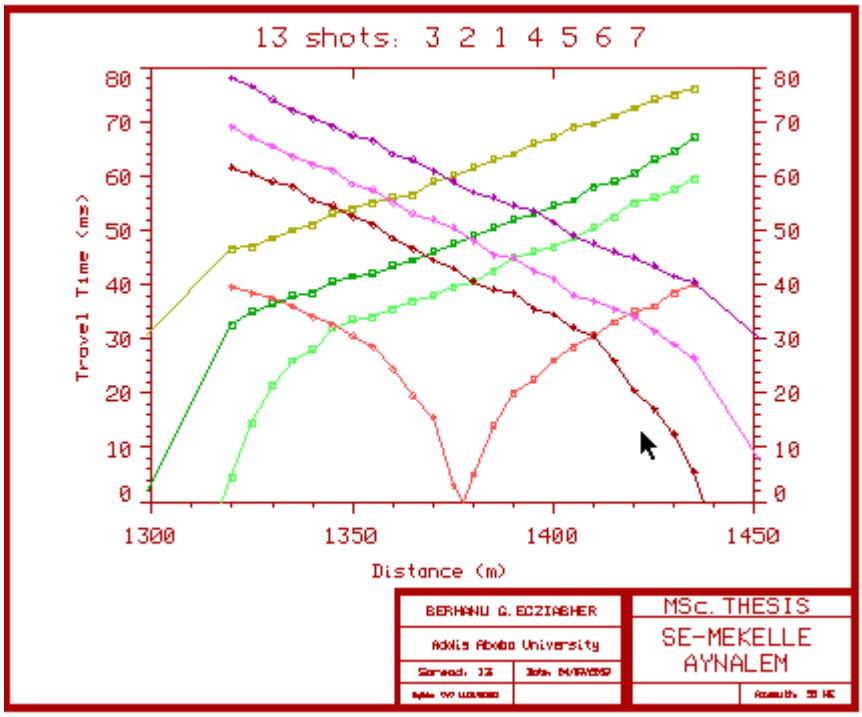

Fig 4.12 Travel time curves for the seven shots in one spread.

The next step was to assign the arrivals on the travel time curves to layers (fig 4.13) so as to determine the apparent velocity for each of the layers. This was the most difficult and crucial step. Then, the reciprocal time information was checked to make sure that they are correct; otherwise the results will be erroneous and inconsistent.

The optimum XY value was selected for the GRM analysis (Palmer, 1980), for the depth analysis and the velocity distribution in each refractor or layer.

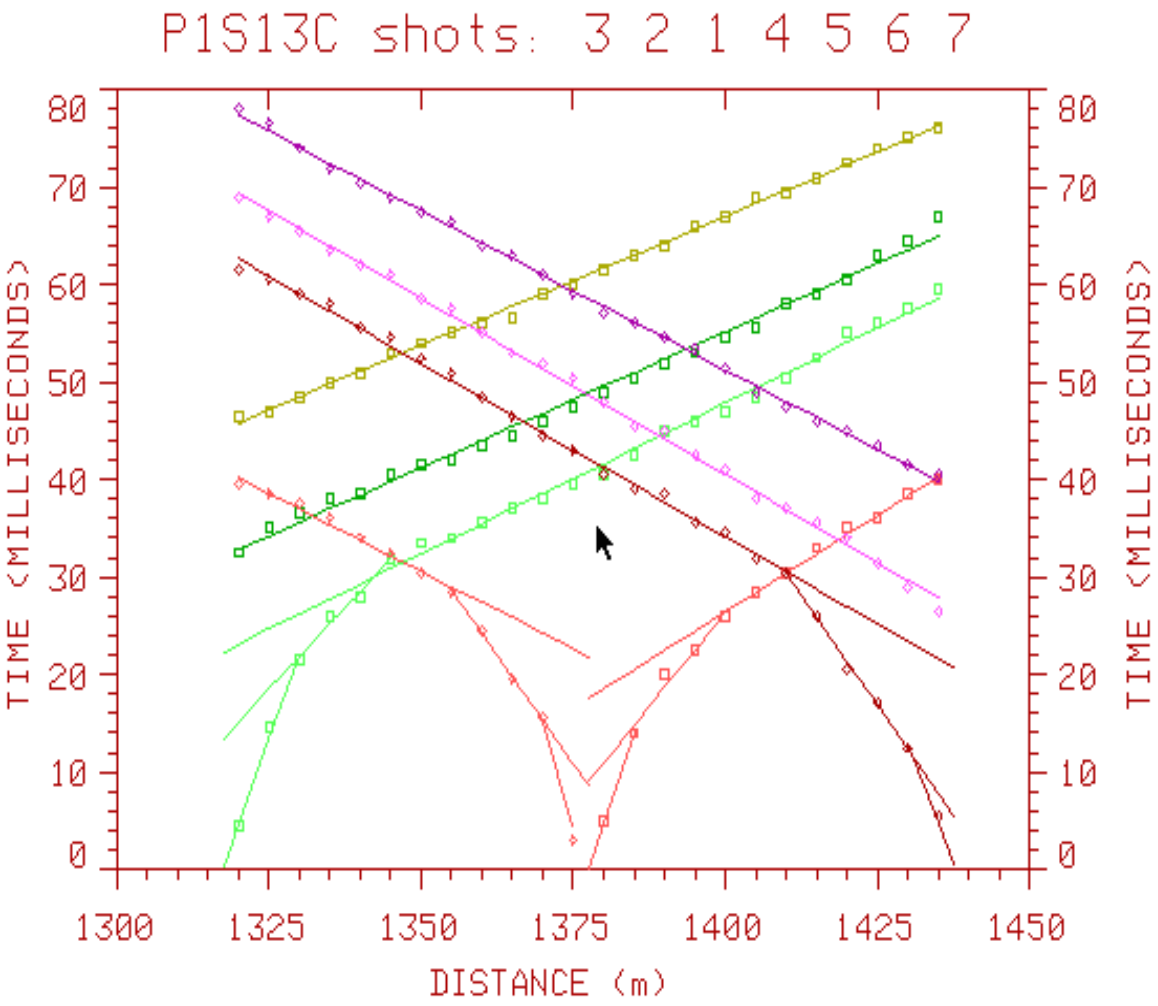

Fig 4.13 Example of arrival time curves assigned to three layers.

Finally the velocity and depth sections of the spread were presented (fig 4.14).

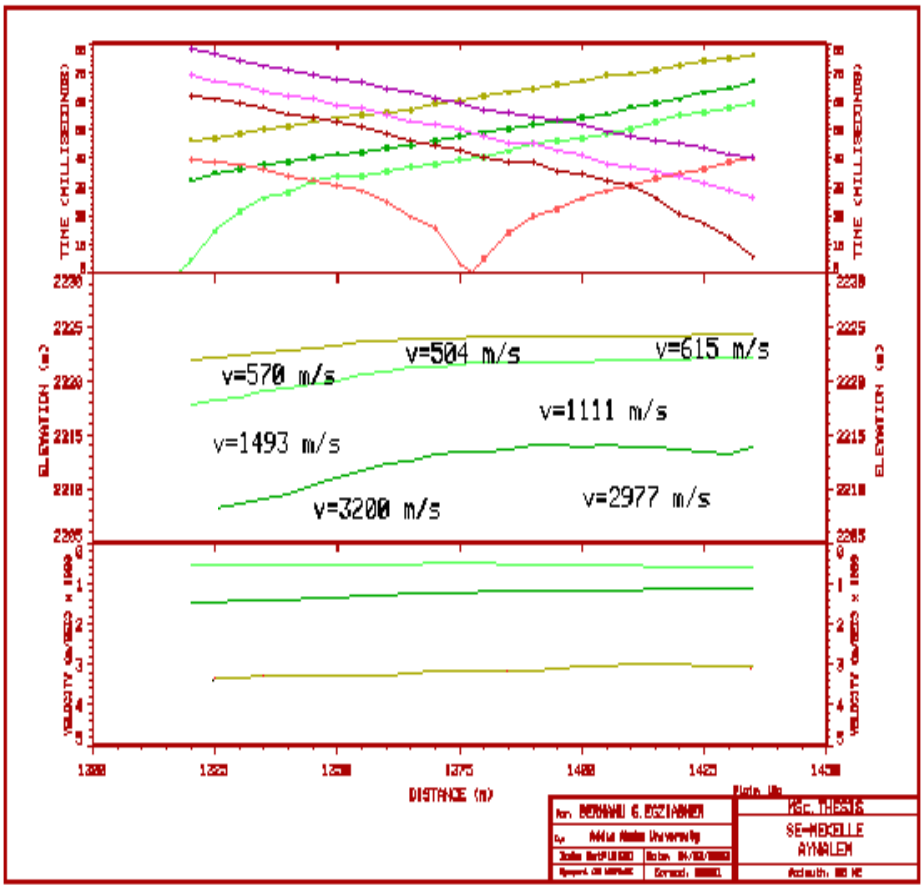

Fig 4.14 Inverted depth and Velocity sections of a spread.

Then the velocities of different layers with their respective thickness for each spreads merged to form the seismic profile sections as shown in figures 4.15 (a), (b), (c), and (d) using the seismic refraction data processing software GREMIX^{TM} $_{V\,2}$ (Interpex ltd).

Fig 4.15 Merged spreads along the four seismic profiles (a to d)

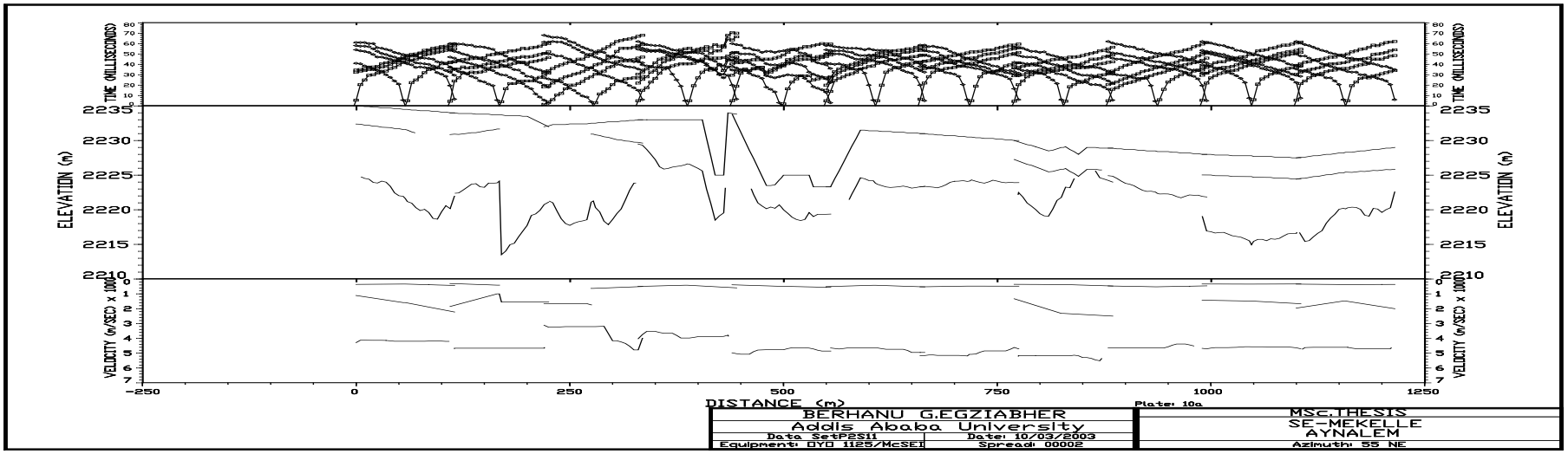

a) Along profile-1 (11 spreads)

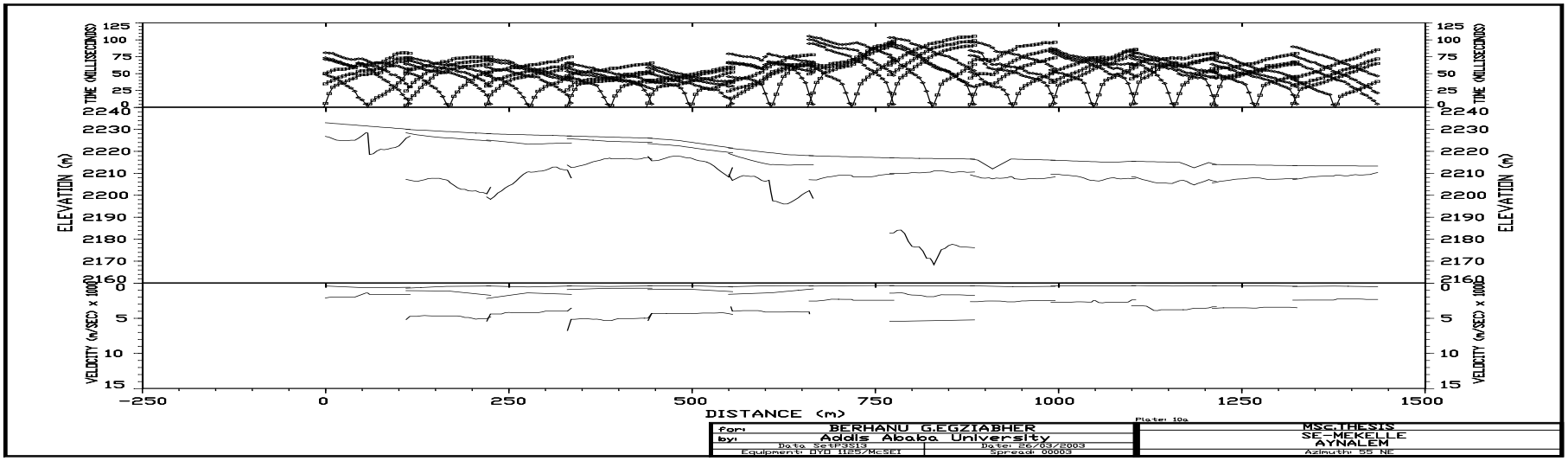

b) Along profile-2 (13 spreads)

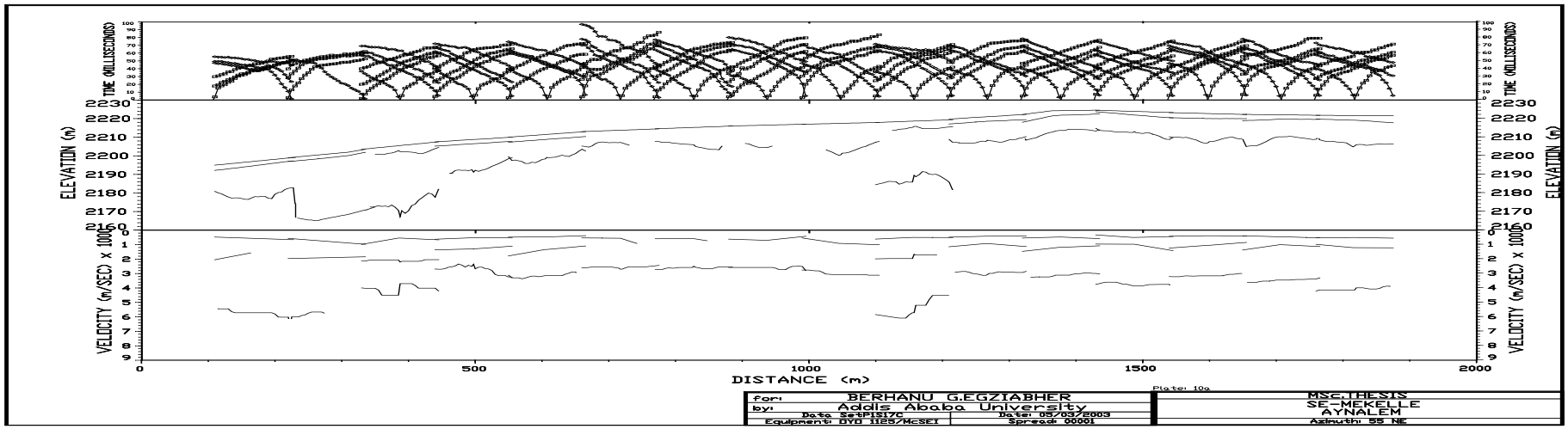

c) Along profile-3 (17 spreads)

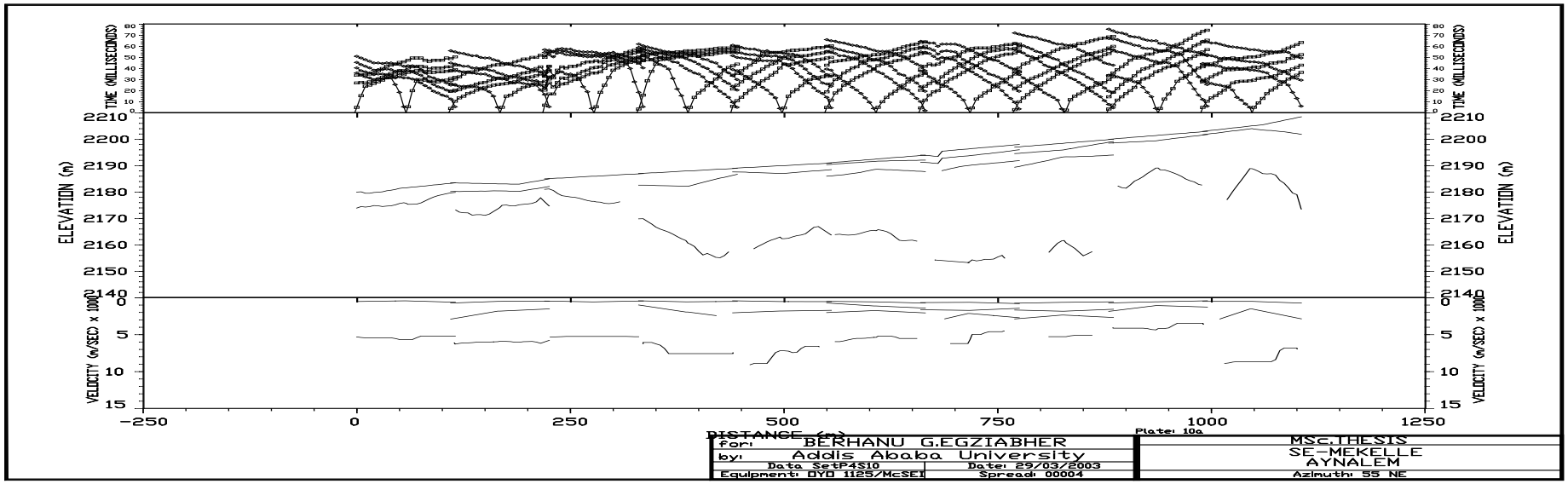

d) Along profile-4 (10 spreads)

4.2.4.4 Results and Interpretation of seismic refraction

According to the velocity distribution, four seismic layers have been identified. The first layer is with velocity less than or equal to 600 m/s. This layer is found in all spreads and it is interpreted as the soil cover.

The second seismic layer in the area has velocity between 900 m/s and 1500 m/s. These are interpreted differently in different parts of the study area depending on the geology, the magnetic and electrical survey results. Accordingly, on profiles 2, 3 and 4 are interpreted as sand layers where as at the end of the first profile between 1000 & 1200 meters (fig 4.16), it is interpreted as a saturated soil horizon.

The third layer has velocities ranging between 2000 m/s and 4000 m/s. These are interpreted as the limestone rock layers. And in some areas, when it is underlain by shallower dolerites like at the end of profile-4 (fig 4.19) and middle of profile-2 (fig 4.17), its velocity is lowered to 1700 m/s. this lower velocity may be related to faulting and fracturing due to the upcoming dolerite dykes from beneath.

The fourth layer has velocity greater than or equal to 4000 m/s. Mostly this is detected at higher depths. But in some places, at the distances located 400 m on profiles-1 & 2 (figs 4.16 & 4.17), and at the beginning & end of profile-4 (fig 4.19), it is found at shallower depths. This is evidenced by the geology field observation as dolerite outcrops.

From the seismic profile sections, some displacements at distances of 300 & 1000 meters of profile-1, at 300 & 850 meters of profile-2, at 450 & 1050 meters of profile-3,and 1000 m of profile-4 are interpreted as normal faults. All these interpreted faults are associated with the dolerites at shallower depths and they are also directly correlated to the lineaments and weak zones detected by the magnetic survey (fig 4.25,b and fig 4.26,b).

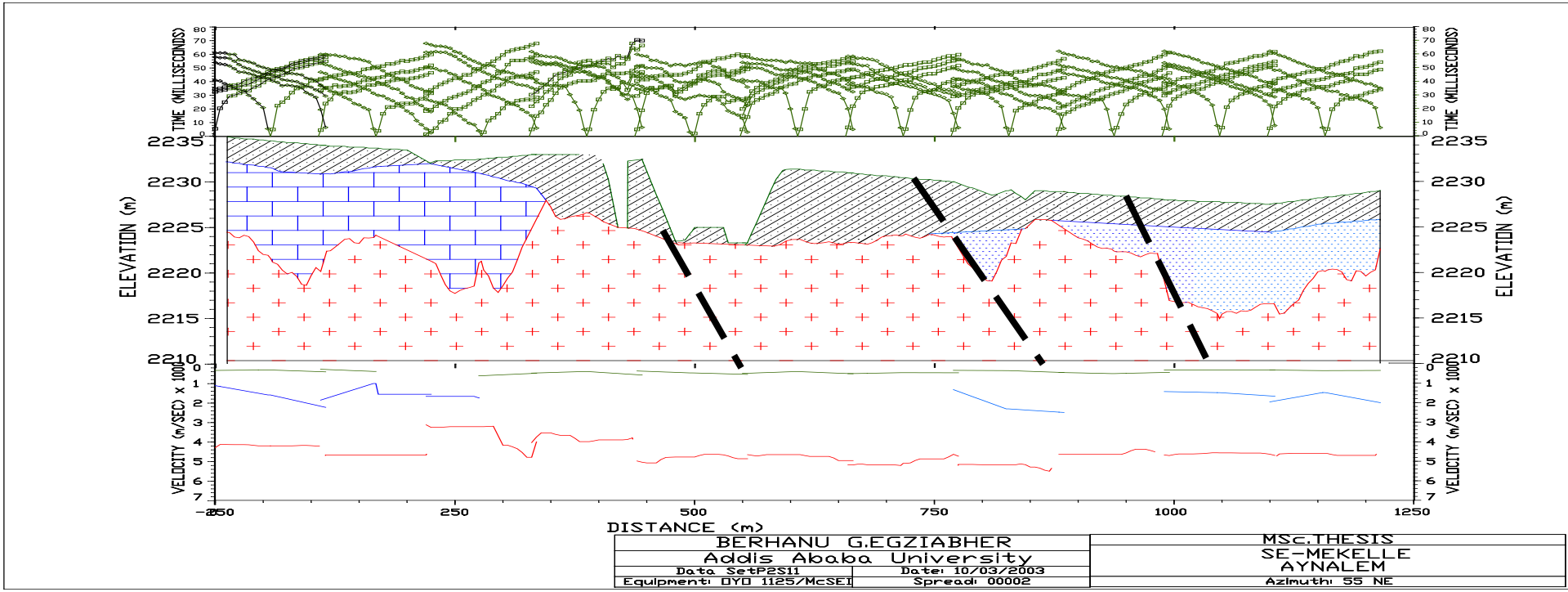

Fig. 4.16 Seismic section along profile-1 (from NE to SW direction)

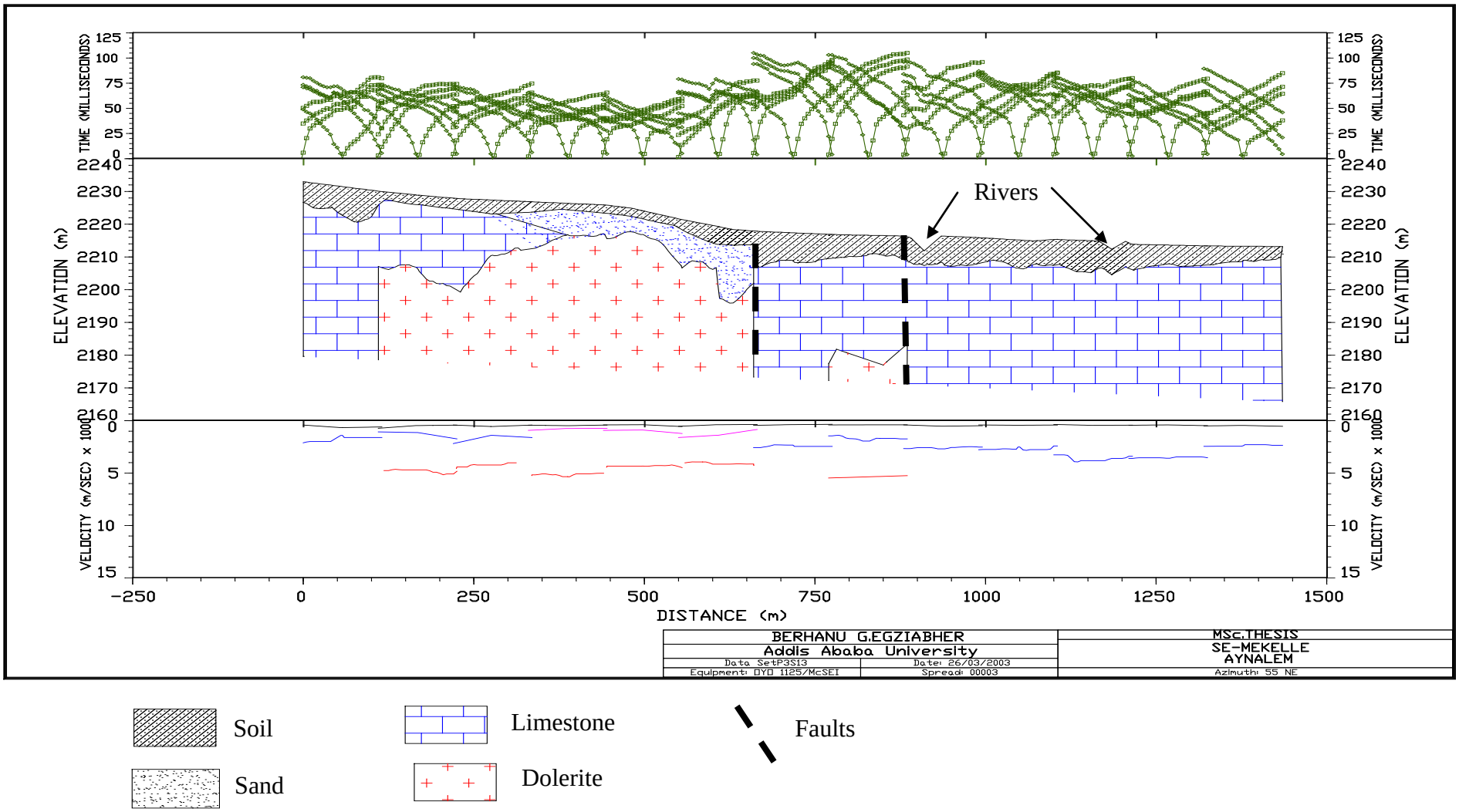

Fig. 4.17 Seismic section along profile-2 (from NE to SW direction)

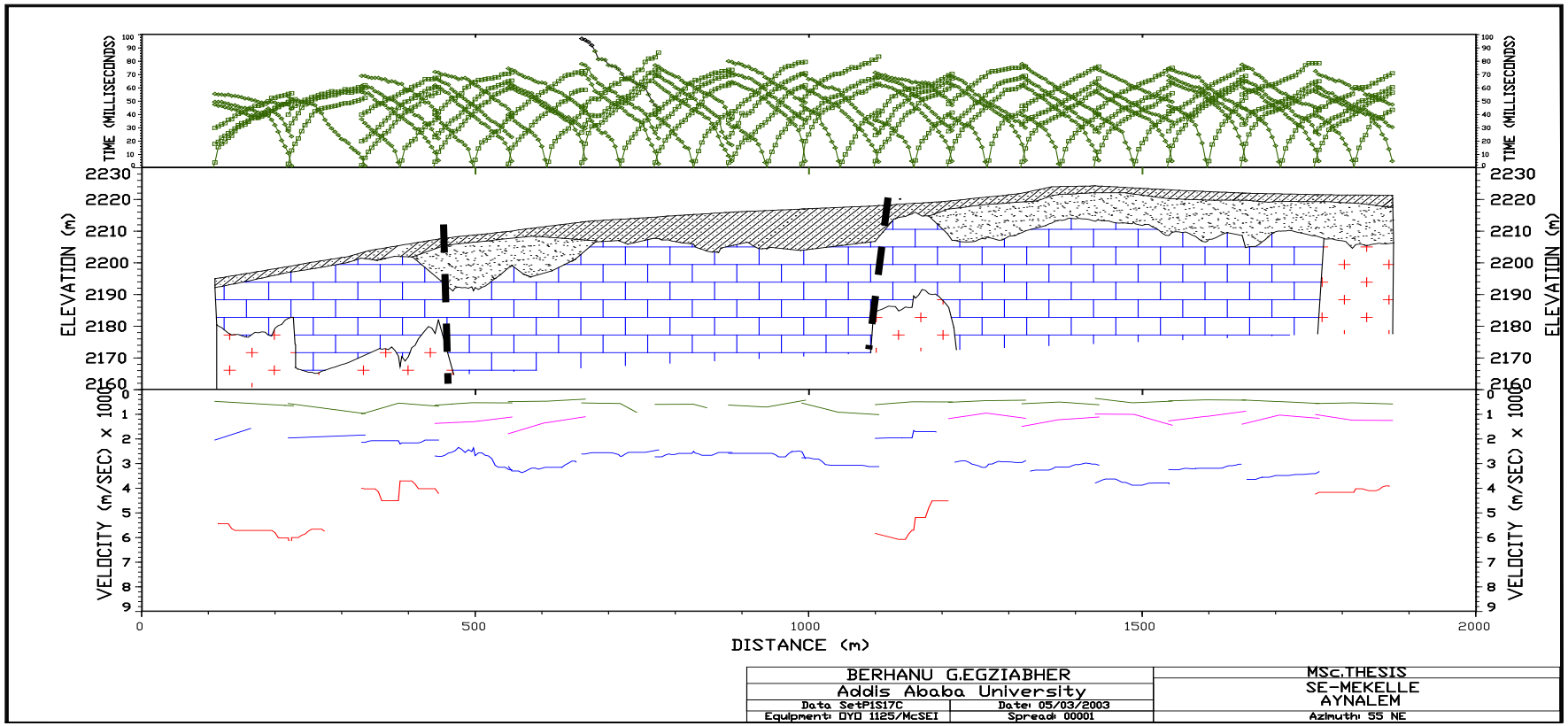

Soil

Sand

Limestone

Dolerite

Faults

Fig 4.18 Seismic section along profile-3 (from SW to NE)

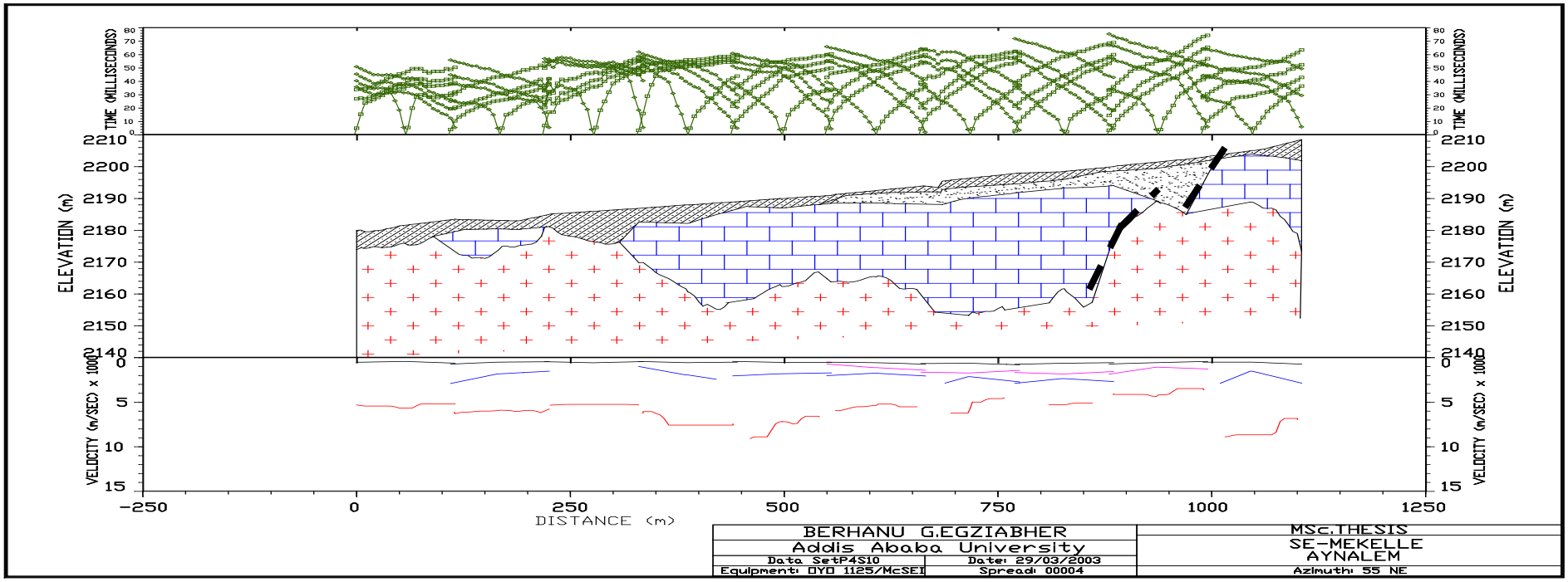

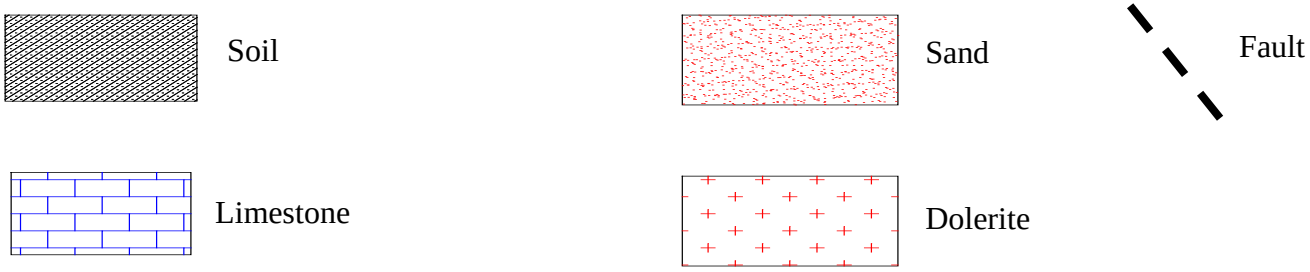

Fig.4.19 Seismic section along profile-4 (from SW to NE direction)

4.3 Magnetic Survey

4.3.1 Basic Principles of Earth's Magnetism

4.3.1.1 The nature of Magnetism

About four centuries ago, the English scientist William Gilbert, explained why the compass points towards north by proposing that the earth itself is a large magnet.

The basic principle is based on ideas about how magnets interact with one another and about how magnetism is produced.

The eighteenth century French physicist Charles Coulomb described the interaction of magnets in terms of forces acting at points called Magnetic Poles. Every magnet possesses a positive and negative pole, so named because of their opposite effects on the poles of another magnet.

The force F acting on two poles having values of pole strength P_1 and P_2, and separated by a distance r, is expressed by Coulomb's Law,

$$F = \frac{1}{\mu}\frac{P_1 P_2}{r^2} \quad \text{.....(51)}$$

Where μ represents the magnetic permeability, which is a property of the medium where the magnets are located.

The two poles of a magnet act oppositely but with equal pole strength. It is not possible to separate or extract either of these poles. To break a magnet is to immediately create two new magnets, each with a positive pole and a negative pole. For this reason we commonly use the word dipole to describe a magnet.

Because a magnet has the capacity to exert force on other magnets or iron objects, it is said to be surrounded by a field of force, which is called its Magnetic Field.

The magnetic field intensity is expressed in units of force divided by pole strength. The basic cgs unit of field intensity is the Oersted.

1 Orested =1dyene/1 unit of pole strength

Since most magnetic anomalies of interest to exploration Geophysicists amount to a very small fraction of one oersted, a subunit called gamma (γ) is more convenient to use. It is defined as

1 gamma=10^{-5}oersted

4.3.1.2 The main magnetic field

According to Robinson (1988), before the time of William Gilbert, there was considerable dispute about whether a loadstone compass was attracted by the earth or by poles of force in the heavens.

Gilbert presented convincing arguments that the attraction came principally from with in the earth.

In 1838, Carl Friedrich Gauss published an elegant mathematical proof that approximately 95 percent of the field must originate inside the earth, but that the remaining 5 percent must be produced by external processes.

Further research revealed that a large part of the interior field is produced in the core of the earth, but that the remaining part has its source in the crust.

Now days, the earth's magnetic field is separated in to the following three parts.

1. **The main magnetic field**, which is produced in the core of the earth and accounts for the very large regional variations in the field intensity and direction. Its source is believed to be the flow of ionized fluid in the outer liquid core where a system of convection currents is assumed to exist.

2. **The external magnetic field,** which is produced by electric currents in the earth's ionosphere consisting of particles ionized by solar radiation and put into motion by the solar tidal force.

3. **The anomalous magnetic field,** which is produced by ferromagnetic minerals in the earth's crust. This magnetic field is of principal interest to exploration geophysicists and the external field fluctuates in daily cycles is corrected as diurnal corrections during a magnetic survey.

The magnetic field on the earth's surface is strongest in the Polar Regions where maximum intensity is close to 70,000 gammas and diminishes to an average of about 30,000 gammas near the equator.

Inclination is vertical ($I=90^0$) at the location of 75^0 N,101^0 W in northern Canada, & at the location of 65^0 S, 143^0 E in Antarctica. These locations are called the north and south magnetic poles. The contour of zero inclination is called the magnetic equator.

4.3.2 Data Acquisition, Processing, and Interpretation

4.3.2.1 Instrumentation

The instrument used during the survey was a Scintrex made proton precession magnetometer IGS-2/EM. This instrument is simple to operate and portable. The total strength of the magnetic field at a station is measured by the instrument with out measuring its direction.

4.3.2.2 Data Acquisition

Measurements were taken at station intervals of 12 meters along four survey lines about 1.5 kms apart, as indicated in fig (4.1). But the station intervals of survey line-1 was 6 m for the first 128 stations in order to detect suspected fractures and the rest 51 stations were made at intervals of 12 meters like the other three profiles.

Measurements were taken at 799 observation stations that cover about 8.8 km along the four survey lines.

Each survey lines have different lengths. The shortest (profile-1) is about 1380 meters and the longest (profile-3 with 245 stations) is 2940 meters long. The length of the lines is dictated by the accessibility.

At each station, time is recorded when each field intensity measurements is made. Readings were also taken periodically at a base station. These times and readings of the base station are used later to make corrections for diurnal variation.

4.3.2.3 Data correction

From careful examination of geomagnetic records, the strength of the earth's magnetic field changes over the course of a day. This daily fluctuation is called diurnal variation. It occurs mostly during the daylight hours. This is because ionization occurs during the daylight hours when a portion of the ionosphere is exposed to direct solar radiation.

It is known that the diurnal variation is strongest in the equatorial region and diminishes at higher latitudes.

A base station was established for each survey line for the purpose of determining time corrections. The measurements were consequently corrected for time dependent variations, and field intensity values were calculated in all of the four survey lines.

The curves of time versus total magnetic field measured by taking periodical readings at approximately one-hour interval at the base station for each of the four survey lines are shown in figure 4.20 below.

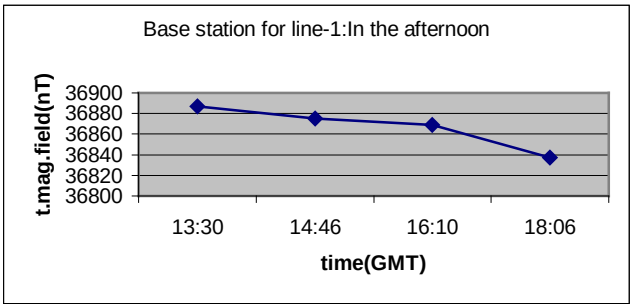

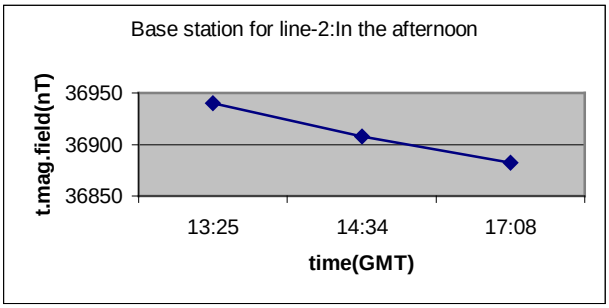

a) b)

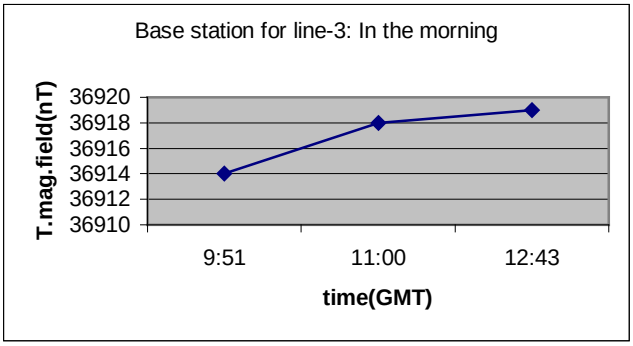

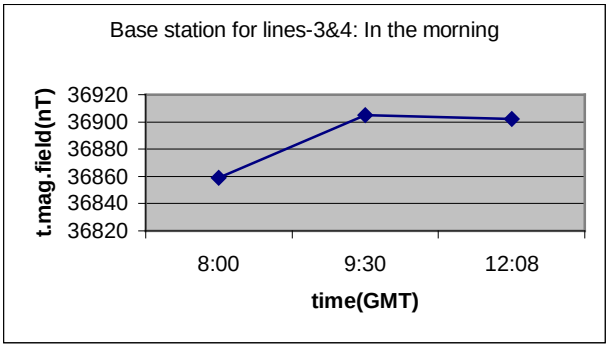

c) d)

Fig 4.20 Total Magnetic Field Strength versus Time curves for the base stations of P-1 (a), P-2 (b), P-3 (c), & P-4 (d).

As indicated in the figures two of the survey lines (lines 1 & 2) were made in the afternoon. The diurnal variation curves of these two base stations show a decrease from 12 to 18 hours GMT. The other two survey lines (lines 3 & 4) made in the morning show rising of the curves until 12

am GMT. This indicates that the diurnal variation attains its maximum value at noon time (Robinson, 1988).

4.3.2.4 Data processing and presentation

The magnetic field intensity values, which have been corrected for time-dependent variations, combine both the main field and the anomalous field.

Four profile curves, a contour map, and a color display image of the anomaly patterns are shown in figures 4.21, 4.22, 4.23, 4.24, 4.25, and 4.26.

4.3.2.5 Results and Interpretation

Profile-1:

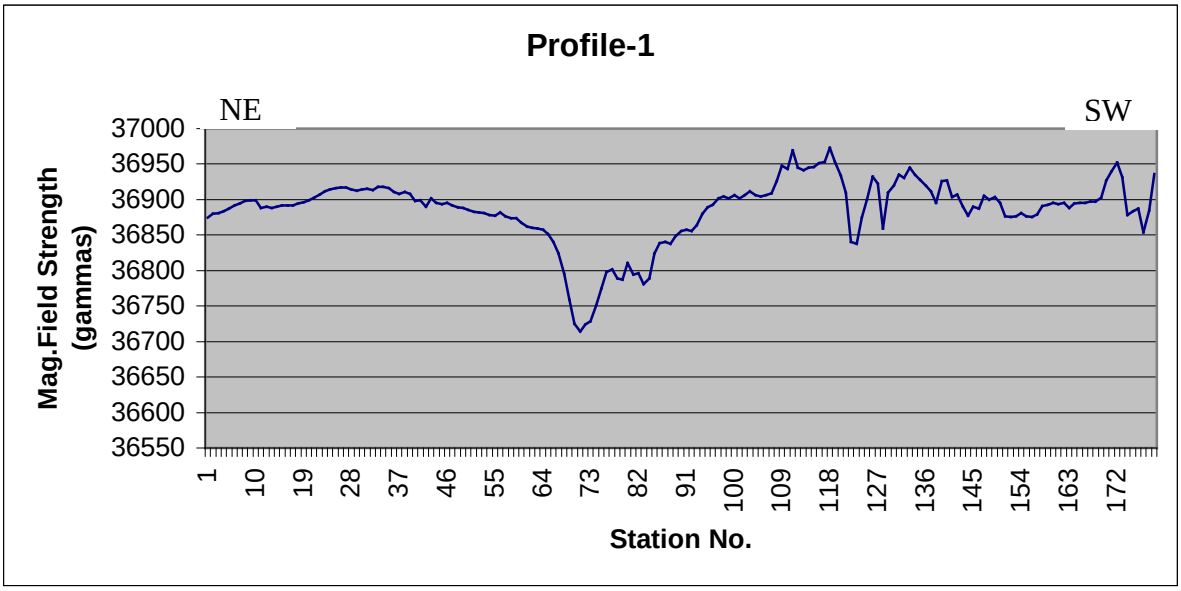

Fig 4.21 Magnetic Intensity variation along profile one.

Along this profile, the curve starts to rise a little bit at station number 19. This is the area between the shale-marl rock unit and the limestone rock exposures. At this point a contact is expected between these two rock units. The strength of the field declines to 36714 gammas at station number 71 where water starts to appear from the highly fractured and weathered dolerite rock unit exposed at the river course. The dolerite abruptly stops exactly at the place where the water comes out and the fractures are aligned in $N60^0W$ direction. Both from field information and the magnetic field pattern we can conclude the presence of fault or fracture zone at that point or station.

At station 123, which is at the river margin, there is observed a slight decline in the magnetic field strength due probably to presence of fracture or weak zone. As it was confirmed from the seismic refraction, geologically dolerite is expected beneath the thick soil deposit at this place.

Maximum field strength of 36970 gammas is observed between stations 108 and 118. This could be due to the dolerite dyke just beneath a thin soil cover.

Although the area after station 120 is covered by thick soil and smoother in topography, the profile curve shows irregular anomalies. This may be due to the fact that the rock formation overlain by the thick soil deposit is very altered and fractured. This may indicate the area to be rich in groundwater or the groundwater table is nearer to the surface. The wet grassy land and the presence of many springs on one side of the river margin give strength to the above conclusion. The presence of water in that area is also confirmed by the result of seismic refraction survey.

Profile-2:

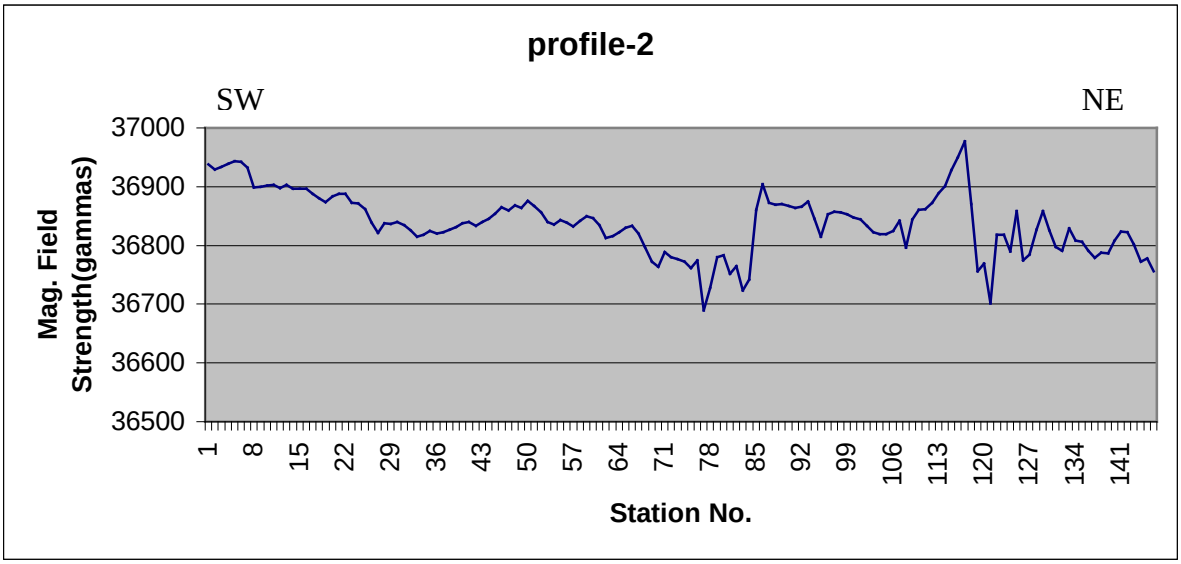

Fig 4.22 Magnetic Intensity variation along profile two.

In profile-2 fig 4.22 the curve steadily declines until it reaches the lowest level at stations 77 and 84. In this region, which is located about 100 m west of Pumping Well-2, faults associated with shallower depth dolerite rocks were detected by the seismic refraction as shown in fig (4.17).

The lower value at station 121, exactly the place where the dolerite ridge starts may be due to the vertical contact between the limestone and the dolerite rock units thereby representing a weak zone. This same point is interpreted as lineament on the contoured anomaly map (fig 4.25).

Maximum field strength of 36910 to 36991 gammas are observed between stations 86 and 117. This could be due to the presence of power lines that passes across the survey line. Exactly at

station 86 and 117, buried pump lines that passes from the boreholes PW2 (at station 86) and from PW8 (at station 117) are located from the field observation.

Profile-3:

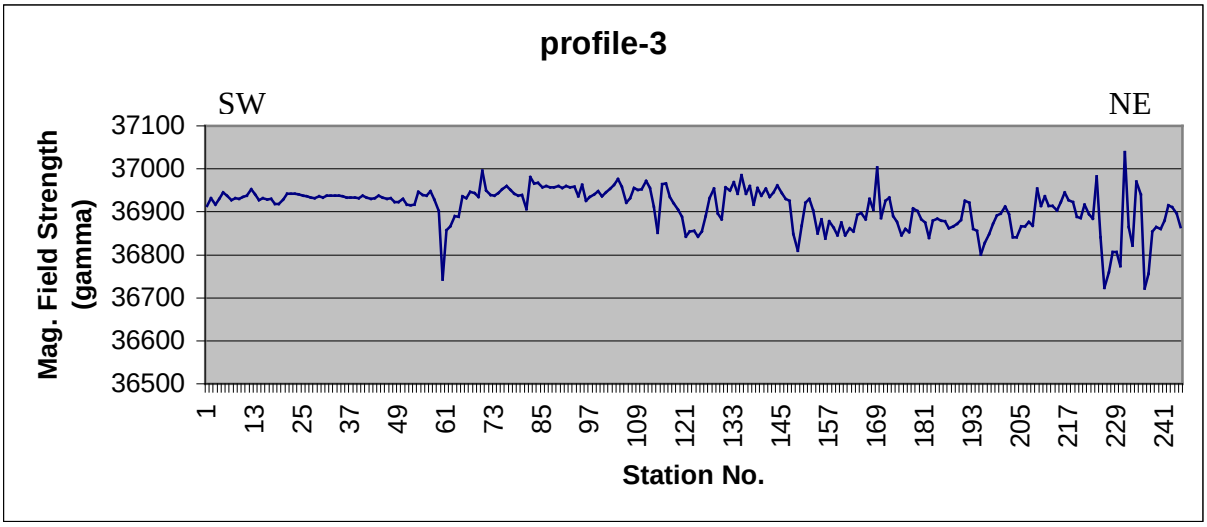

Fig 4.23 Magnetic Intensity variation along profile three.

At the first 14 stations of profile-3, where an outcrop of fractured limestone is observed, the curve shows some fine irregularities. This may be due to the presence of very shallow fractures.

Minimum field strength of 36743 gammas is observed at station 60. This may be due to fracture or fault. This can be seen as small displacements on refraction seismic section of the same profile at about 500 m (fig 4.18).

At station 227, where the margin of the dolerite hill starts, the strength value declines to 36760 gammas. This is interpreted as a fault, which is a continuation from that of profile-2.
Similarly, the lower values at stations 124, 149, 198, and 232 are interpreted as fractures or weak zones.

Maximum field strength of 37040 gammas is observed at station 231 on the dolerite ridge. This may be the presence of massive dolerite dyke beneath it. And similarly, 37003 gammas are recorded at station 169. This is interpreted as the presence of the buried pump line that passes from the pumping wells.

The relatively higher values of the curve between stations 75 and 145 could be due to the presence of a power line, which is almost parallel to profile.

Profile-4:

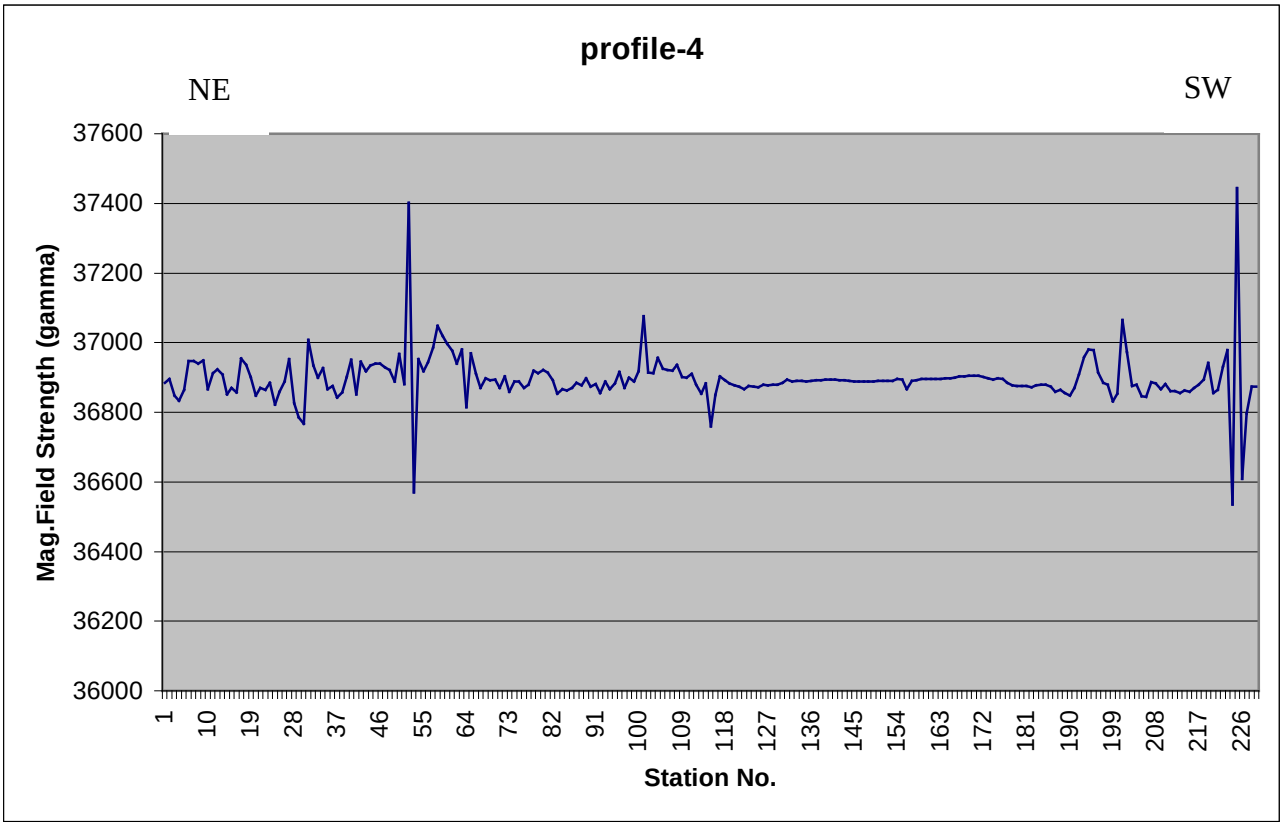

Fig 4.24 Magnetic Intensity variation along profile-4

In this profile two extreme magnetic intensity values are observed from the curve.

At stations 52 and 225 the highest magnetic intensity values of 37401 and 37444 gammas were measured on the dolerite outcrops respectively. These may be probably due to the presence of massive and fresh small-scale dolerite dykes or due to buried iron objects.

And the minimum values observed at stations 53 and 224 (near to the extremely highest values) are 36571 and 36536 gammas. Probably this is due to the presence of very deepest fractures or vertical contacts between the dyke and the other rock formations.

At station 101 a value of 37076 gammas were measured exactly at the location of the buried pump line. And the lower field strength of 36760 gammas at station 115 is located near a small outcrop of fractured limestone inside the sandy soil. Therefore, this is interpreted as a fault. The refraction seismic section at 1000 m of the same profile (Fig 4.19) confirms this fault.

The area between station 116 and 185 shows almost constant values. This implies the absence of small or large-scale fractures and from the geologic & refraction seismic information the area is covered by sandstone that overlies the limestone.

Between stations186 and 199 an outcrop of fractured black limestone is observed and exactly at station 200 dolerite outcrop starts. Thus, the lower field strength of 36831 gammas may be due to the vertical contact between the black limestone and the dolerite.

The magnetic field intensity maps:

Fig 4.25 & 4.26 show the total magnetic field intensity map of the study area prepared using 799 observation stations.

The image and contour maps indicate the total magnetic field variation (anomaly) ranging from 36700 to 37000 gammas in the study area. The trend and orientation of the iso-magnetic contours

are generally NW- SE that is consistent with the trend of geological structures that are almost perpendicular to the survey lines.

The alignments and patterns of these linear anomalies indicate structural trends that may be directly correlated to structural features on a geologic map. Figures 4.25(b) and 4.26(b) show the interpreted faults and fractures from the magnetic field intensity anomaly contour map and from that of the displayed image.

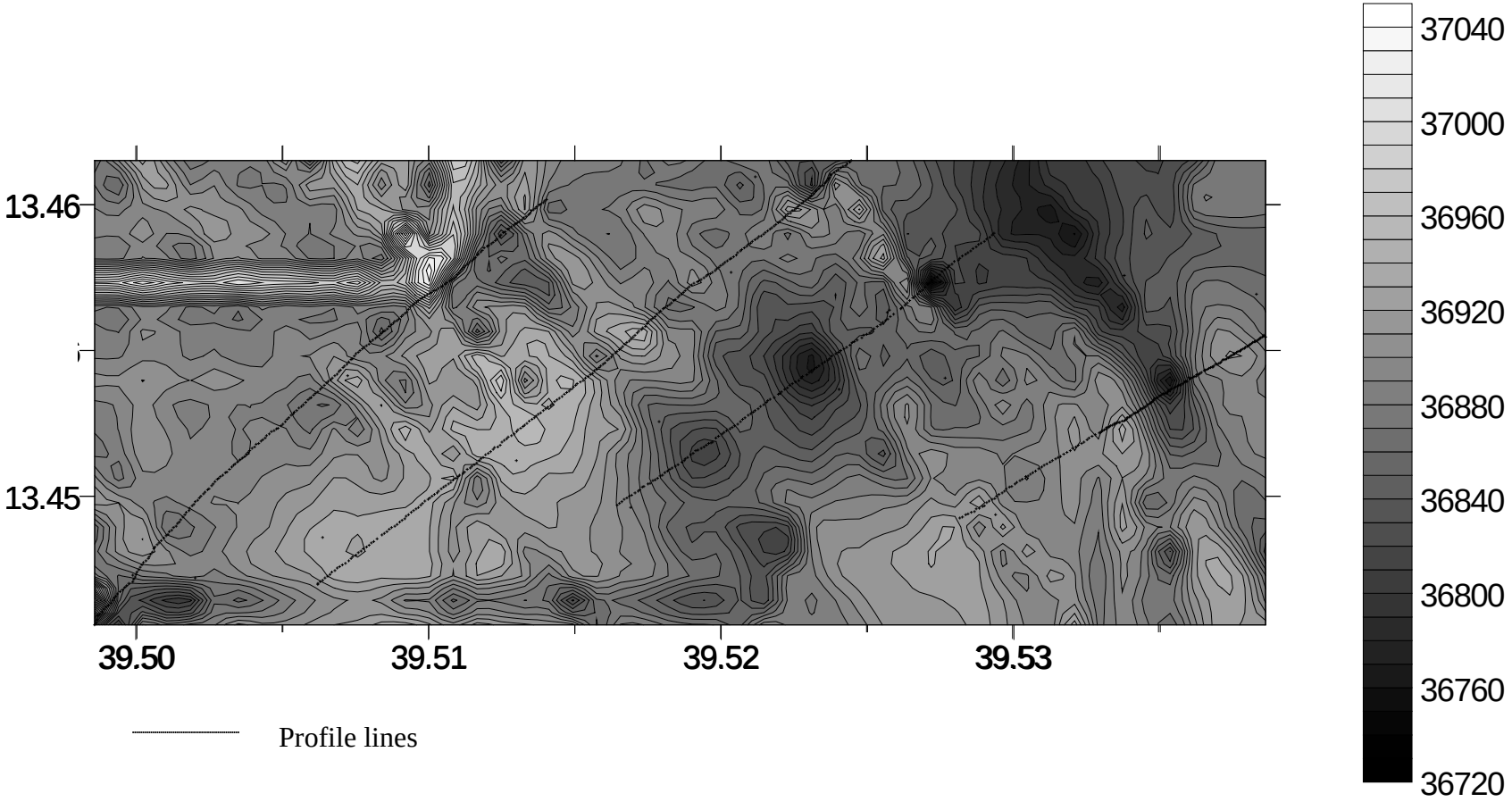

Fig 4.25 (a) Magnetic intensity contour map

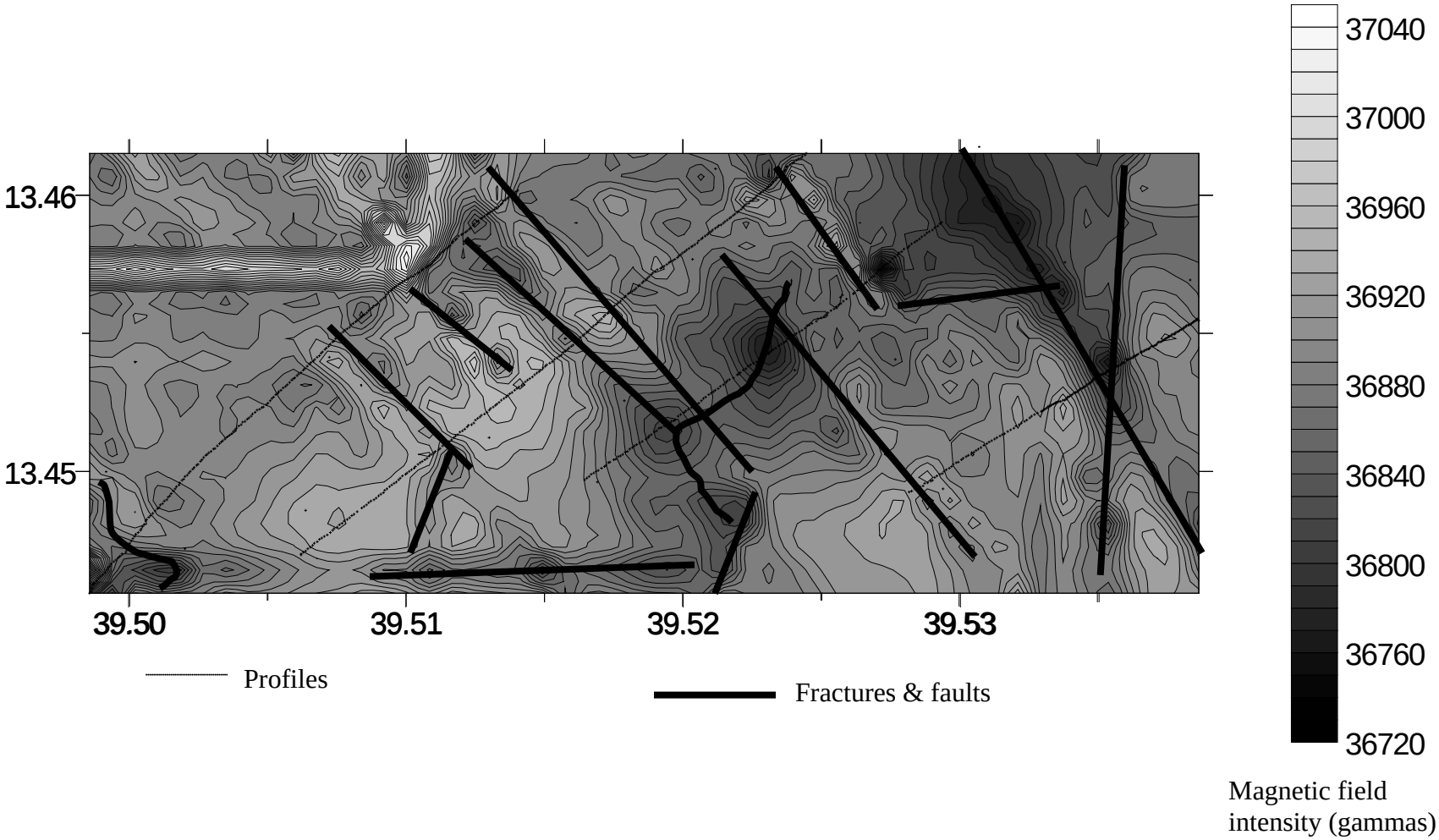

Fig 4.25(b) Interpreted faults and fractures from the magnetic anomaly contour map

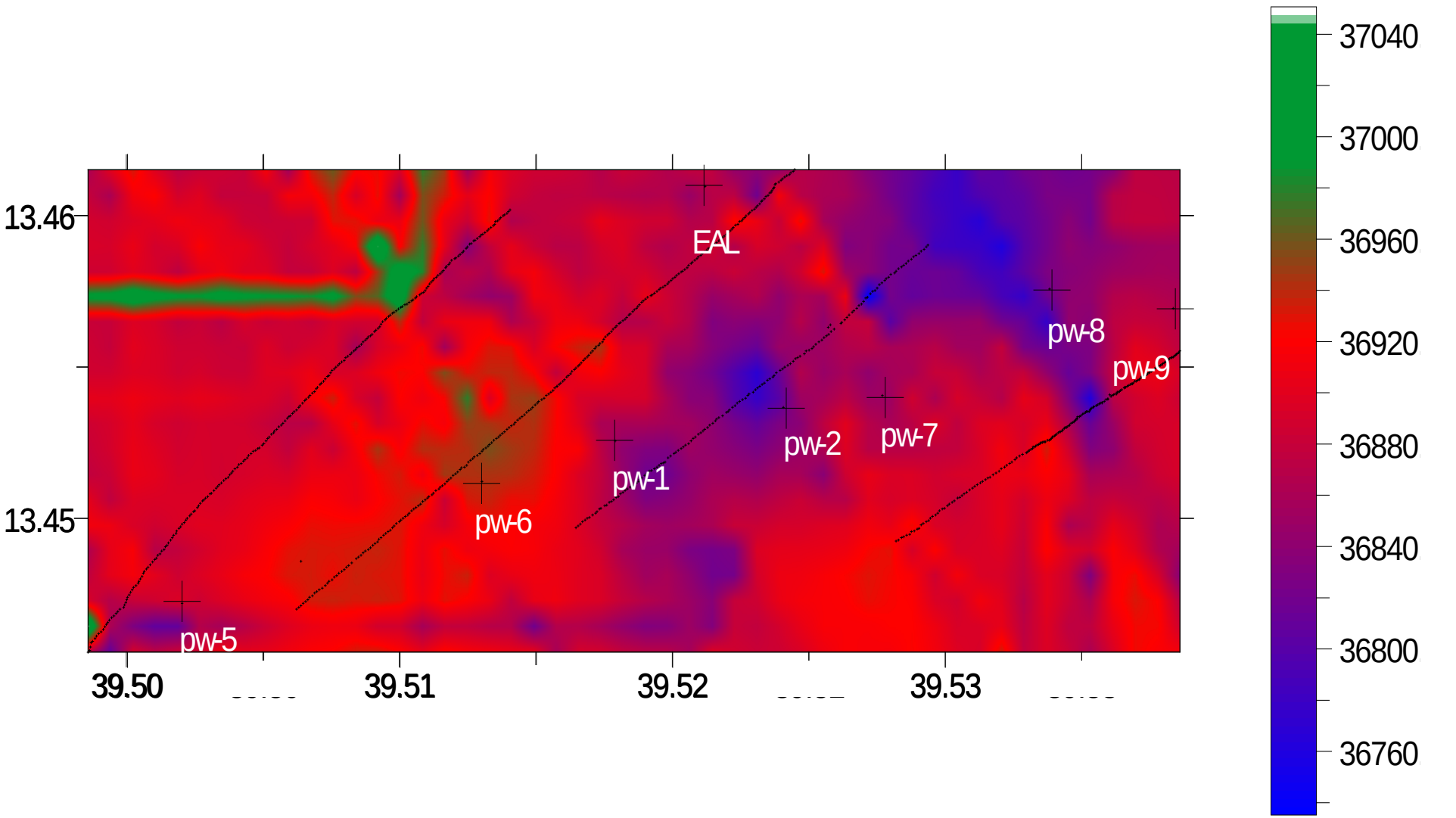

Fig 4.26(a) Image of the magnetic intensity anomaly map

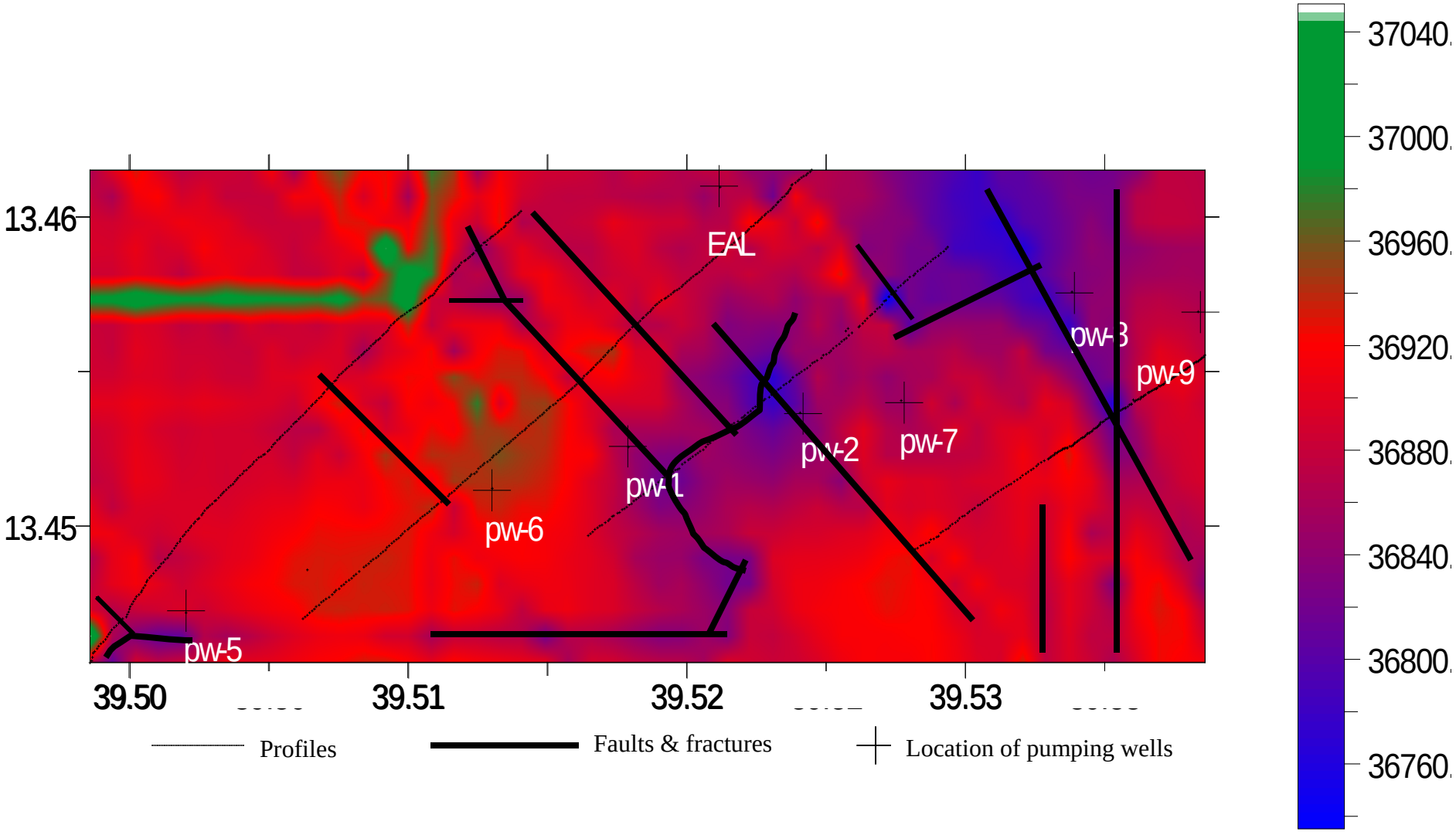

Fig 4.26(b) Interpreted geologic structures from the image of the magnetic intensity anomaly map

4.4 Electrical Resistivty Survey

4.4.1 Theories and General Concepts

The applications of resistivty surveys are very wide. Some of the most important successes of the resistivty method are applications related to groundwater explorations and contamination of normal groundwater, to map buried stream channels, karstic features & caverns and so on. So to understand how it works, it is necessary to start from the basic concepts of resistivty briefly. Most of this theoretical part is taken from standard geophysical books such as Robinson (1988), Burger (1992), and others.

4.4.1.1 Ohm's Law and Resistivty

In 1827 George Simon Ohm reported the following relation ship between resistance (R), curruent (I), and the corresponding change in potential V:

$$V = IR \ldots\ldots\ldots\ldots\ldots\ldots\ldots\ldots\ldots\ldots\ldots\ldots\ldots (53)$$

This relation ship is known as Ohm's law.

Suppose the resistor is made from a rectangular bar of length L and square cross-sectional area A. we can represent the electric current flowing through this resistor by uniform distribution of charges moving along parallel paths from one end to the other. The resistance R of this resistor is described in terms of the length L of the path followed by a charge, the cross sectional area A over which the charges are uniformly distributed, and the resistivty ρ, which is a physical property of the substance used to make the resistor;

$$R = \rho \frac{L}{A} \quad \text{.....(54)}$$

By rearranging this expression, we can express resistivty as

$$\rho = R \frac{A}{L} \quad \text{.....(55)}$$

This implies that ρ is expressed in units of resistance x length. The common units used in exploration geophysics include the ohm-meter, ohm-centimeter, and the ohm-foot.

We see from equation (54) that lengthening the resistor so that charges must travel longer paths through it can increase resistance. The cross sectional area can also be decreased, which impedes the movement of charges by crowding them into a smaller volume.

The concentration of charge passing through a cross-sectional area of the resistor is expressed by the current density, which is

$$\mu = \frac{I}{A} \quad \text{.....(56)}$$

4.4.1.2 Current Flow In Three Dimensions

Suppose that we make up an electric circuit in which the earth is the resistor. We can connect electrodes at two different locations to the battery terminal as shown in fig 4.27.

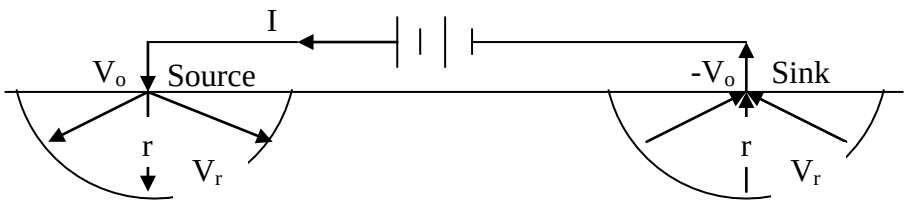

Fig 4.27 Current lines radiating out from a source electrode and converging on a sink electrode.

The electrode connected to the positive terminal is called the source, and the electrode connected to the negative terminal is the sink.

Because of the difference in potential between these electrodes, current is compelled to flow along paths leading from the source to this sink. To find the directions of these paths, we begin by considering separately the effects of the source and the sink. Then we can combine these effects to determine the pattern of three-dimensional current flow in the earth.

To keep things as simple as possible, we will start by assuming that resistivty is constant through out our model of the earth.

The source electrode is positively charged. Therefore, it repels positive electric charges, pushing them outward in to the ground. The implication is that electric current flows outward from the source into the ground. Because the resistivty is uniform, current moves away from the source, radiating outward and uniformly in all directions as shown by the paths in fig 4.27.

Let us consider the resistance encountered by current that has flowed a distance r from the source. Because it spreads out ward in all directions, it has moved through a hemispherical zone. Let us think of this zone as resistor. The current flows out of this resistor when it moves across the area of $2\pi r^2$, which is the surface of the hemisphere. According to equation (54), the resistance R can be expressed by the product of resistivity and the distance r that the current has traveled divided by the area $2\pi r^2$ across which it must flow:

$$R = \rho \frac{r}{2\pi r^2} = \frac{\rho}{2\pi}\left(\frac{1}{r}\right). \quad \text{.....(57)}$$

The change in potential resulting from the flow of current through this hemispherical resistor can be found from Ohm's law:

$$V = IR = \frac{I\rho}{2\pi}\left(\frac{1}{r}\right) = Vo - Vr \quad \text{.....(58)}$$

Equation (58) expresses the difference between the electric potential V_0 at the source and the electric potential V_r at any point in the ground a distance r from the source. The surface of the hemisphere of radius r contains all points at this distance, which means that the electric potential related to current flowing from the source is the same everywhere on that surface. Such a surface is called an equipotential surface.

Next lets look at the effect of the sink electrode. If the potential at the source is Vo, the potential at the sink will be –Vo, for it is connected to the negative terminal of the battery. Because the

negatively charged sink attracts positive charges, we say that current flows toward the sink. Fig 4.27 shows how these charges follow paths that converge on the sink from all directions.

Current flowing from all points at a distance r from the sink must move through a hemispherical zone i.e. identical to a zone with the same radius that surrounds the source.

Thus the difference between the electric potential –Vo of the sink and the potential Vr at all points a distance r away from it, is

$$-V = IR = \frac{I\rho}{2\pi}\left(\frac{1}{r}\right) = Vr - Vo \quad \ldots\ldots\ldots\ldots\ldots\ldots\ldots\ldots\ldots\ldots\ldots\ldots(59)$$

This equation tells us that hemispherical equipotential surfaces are concentric about the sink.

So far, we have analyzed the effects of the source and the sink separately, ignoring interference of the other. But to find the electric potential V at a point in the ground, we must combine the contributions of the source and sink. Using equations 58 & 59, we obtain

$$V = \frac{I\rho}{2\pi}\left(\frac{1}{r_1} - \frac{1}{r_2}\right) \quad \ldots\ldots\ldots\ldots\ldots\ldots\ldots\ldots\ldots\ldots\ldots\ldots\ldots.(60)$$

Where r_1 and r_2 are the distances to the source and the sink to the point (fig 4.27).

4.4.1.3 Potential difference between two points

The resistivity measurements are normally made by injecting current into the ground through two current electrodes C1 and C2, and measuring the resulting voltage difference (ΔV) at two potential electrodes P1 and P2 as shown in fig 4.28.

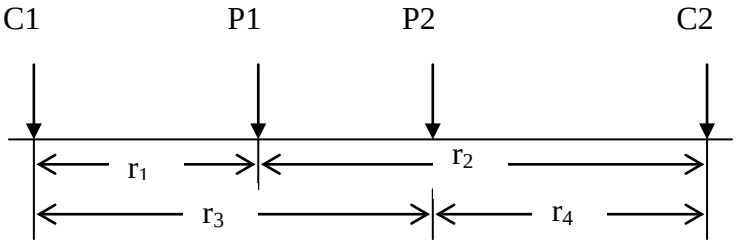

Fig 4.28 Diagram to determine potential difference at two potential electrodes P_1 & P_2

According to equation (60) the potential at P1 is

$$V_{p1} = \frac{I\rho}{2\pi}\left(\frac{1}{r_1} - \frac{1}{r_2}\right) \quad \text{……..(61)}$$

And that at P2

$$V_{p2} = \frac{I\rho}{2\pi}\left(\frac{1}{r_3} - \frac{1}{r_4}\right) \quad \text{……..(62)}$$

So that the potential difference for a point between P1 and P2 is

$$\Delta V = V_{p1} - V_{p2} = \frac{I\rho}{2\pi}\left(\frac{1}{r_1} - \frac{1}{r_2} - \frac{1}{r_3} + \frac{1}{r_4}\right) \quad \text{…….(63)}$$

Therefore, by rearranging for the resistivty.

$$\rho = K\frac{\Delta V}{I} \quad \text{……(64)}$$

Where $K = \left[\frac{2\pi}{\frac{1}{r_1} - \frac{1}{r_2} - \frac{1}{r_3} + \frac{1}{r_4}}\right]$ is called the geometric factor which depends on the arrangement of the four electrodes.

There fore, after arranging the distances between the current and potential electrodes according to some well-known configurations one can determine the resistivty of the ground.

If the array is laid down over a layered earth then the resulting resistivty obtained using equation (64) for any of the different types of configurations is called apparent resistivty. That means the calculated resistivty value is not the true resistivty of the subsurface.

4.4.1.4 Electrode Configurations (arrays)

The most common electrode patterns used in resistivty surveying almost always are the Wenner, Schlumberger, or dipole-dipole.

In **Wenner** electrode geometry the spacing between all electrodes is equal and conventionally it is denoted by the letter a. in fig. $r_1 = r_2 = r_3 = r_4 = a$, thus the Wenner geometric factor becomes $K = 2\pi a$

In the case of **Schlumberger** array, a symmetrical distribution of current and potential electrodes about a central point is employed. But the potential electrodes are spaced much more closely than the current electrodes.

In the **Dipole-dipole** arrangement, the potential electrodes and the current electrodes function independently. Both sets tend to be fairly closely spaced with a significant distance between the sets. Because cable lengths between the electrodes are short, it is much easier to place the potential electrodes at large distances from the current electrodes, thereby facilitating deep investigations.

4.4.1.5 Electrical Resistivty Surveying Procedures

In electrical resistivty surveys, there are two types of operations depending on the parameter to be measured. These are called resistivty sounding and resistivty profiling.

Resistivty Sounding; also called Electrical Drilling or Vertical Electrical Sounding (VES) is a resistivty procedure in which the vertical variation of resistivty of the subsurface is mapped. An electrical resistivty sounding is done at some location by measuring several values of apparent resistivty with successively greater electrode spacing. As the electrode array expands, the same proportion of current is distributed through an increasingly deeper zone.

Resistivty profiling; also called Lateral Inhomogenity Hunting (LIH), is a procedure in which the variation of resistivty in the lateral direction is determined. This is usually done with fixed electrode spacing (like Wenner). A series of apparent resistivty measurements is made by moving

the whole electrode array from place to place along a profile. If values are obtained along several parallel profiles, a contour map of apparent resistivty can be prepared.

4.4.1.6 Electrical Resistivty and the Geological materials

In shallow subsurface, electricity is conducted almost entirely by the fluid present. Thus the resistivty of sediments and rocks in this environment are controlled by the amount of water present and its salinity. Because this conduction is electrolytic and is related primarily to ions moving through the fluid, the cation exchange capacity of clay minerals increases conductivity.

According to Burger (1992), all the following reduce resistivty: increasing water content, increasing salinity of water, and increasing clay content. Assuming that water is available to fill voids, resistivty is lowered by increasing porosity, increasing number of fractures, and increasing weathering. Conversely, increasing compaction and lithification raises resistivty. Because of these factors vary so much in the natural environment, it is not surprising that resistivty vary greatly and that it will be difficult to correlate resistivty with source materials in the absence of other geologic information.

4.4.2 Data Acquisition, processing, & Interpretation

4.4.2.1 Instrumentation

The instrument used during this survey was a Sweden made ABEM TERRAMETER SAS1000. This instrument with one input channel has a Ni-Cd battery pack and in addition it has an

External battery adapter with its DC input cable of using an external 12V battery. The instrument is equipped with a PC-compatible microcomputer controlled by four knobs.

4.4.2.2 Data Acquisition

Resistivty profiling was conducted using Wenner configuration with electrode spacing of 20, 40, and 100 meters along a single profile.

Accordingly observations were taken every 20, 40, and 100 m by moving the whole setup along a profile that covers about 1.5 km in length.

In this survey 76, 39, and 15 resistivty observation stations were taken for 20 m, 40 m, and 100 m spacing respectively.

4.4.2.3 Data processing and presentation

The data, resistance in ohms and milliohms, were changed to apparent resistivty by multiplying with their respective geometric factor of the Wenner array (2π a) using equation (64).

Three apparent resistivty curves are made for different electrode spacing as shown in Fig 4.29(a, b, c, & d).

Fig 4.29 (a) shows the variation of apparent resistivty along the traverse for electrode spacing of 20 m and spread center spacing of 20 m.

Similarly, Fig 4.29 (b) and (c) are variations of apparent resistivty for 40 m and 100 m spread center and a-spacing.

In addition to these three curves, an apparent resistivty section is made by overlapping the three curves for that profile as shown in Fig 4.30.

According to the paper by Edwards (1977), to determine the maximum depth mapped by a particular survey using Wenner array, multiply the maximum electrode spacing “a”, by the appropriate depth factor 0.519. Where “a” is the electrode spacing of the Wenner array.

Based on this, the maximum depth of investigations for the electrode spacing of 20, 40, and 100 meters are about 10 m, 21 m, and 52 meters respectively.

Thus, Fig 4.30 shows the variation of apparent resistivty both laterally along the traverse and along the depths for each “a”-spacing.

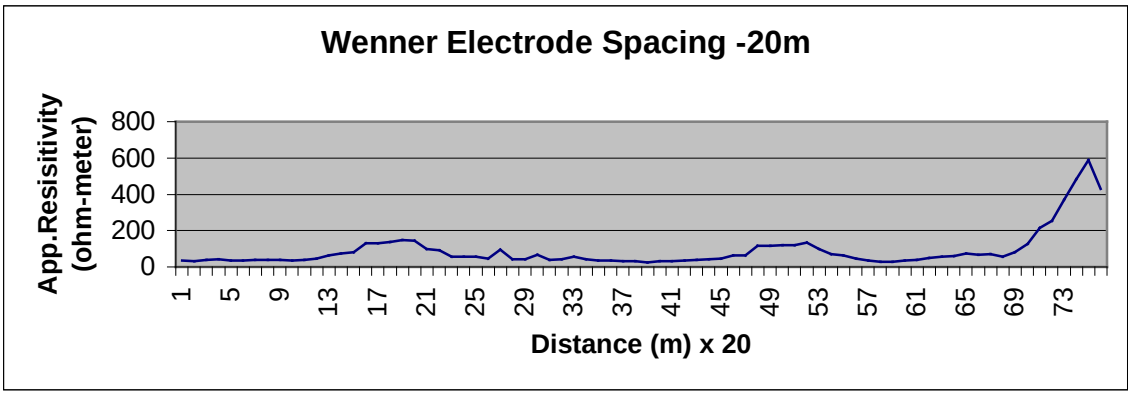

a) Lateral apparent resistivty variation at an approximate depth of 10 m.

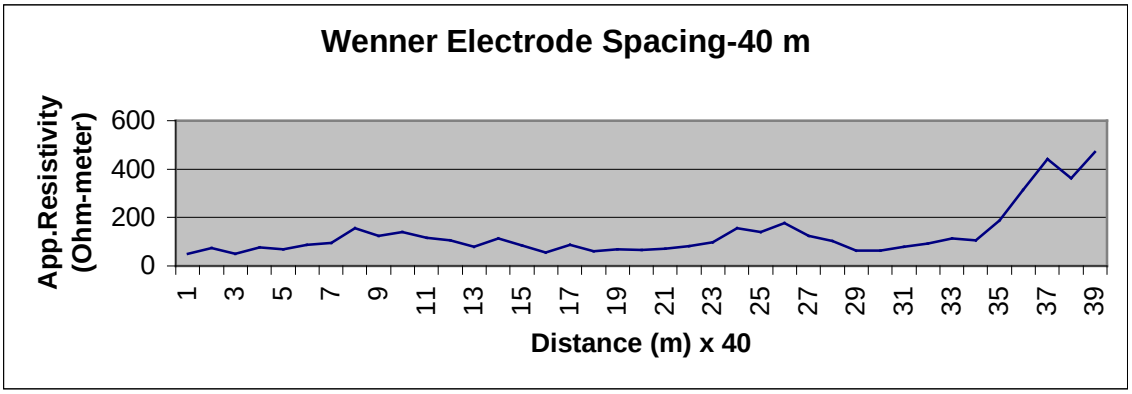

b) Lateral apparent resistivty variation at an approximate depth of 21 m.

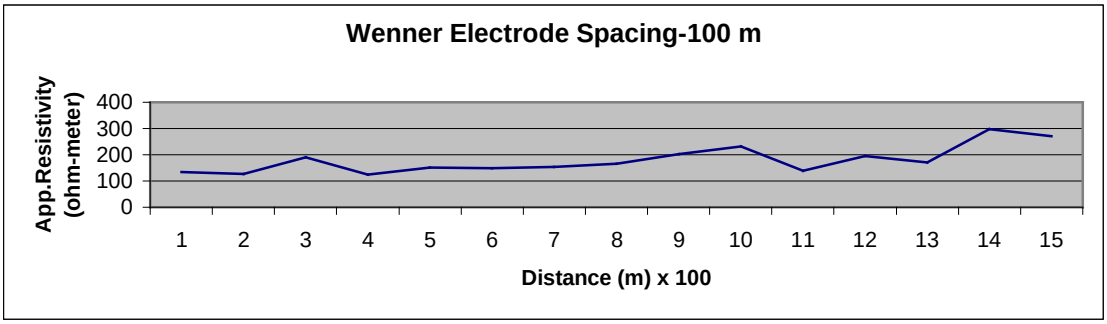

c) Lateral apparent resistivty variation at an approximate depth of 52 m.

Fig 4.29 (a, b, c) Apparent resistivty variation curves along the same profile but with different depth of investigations

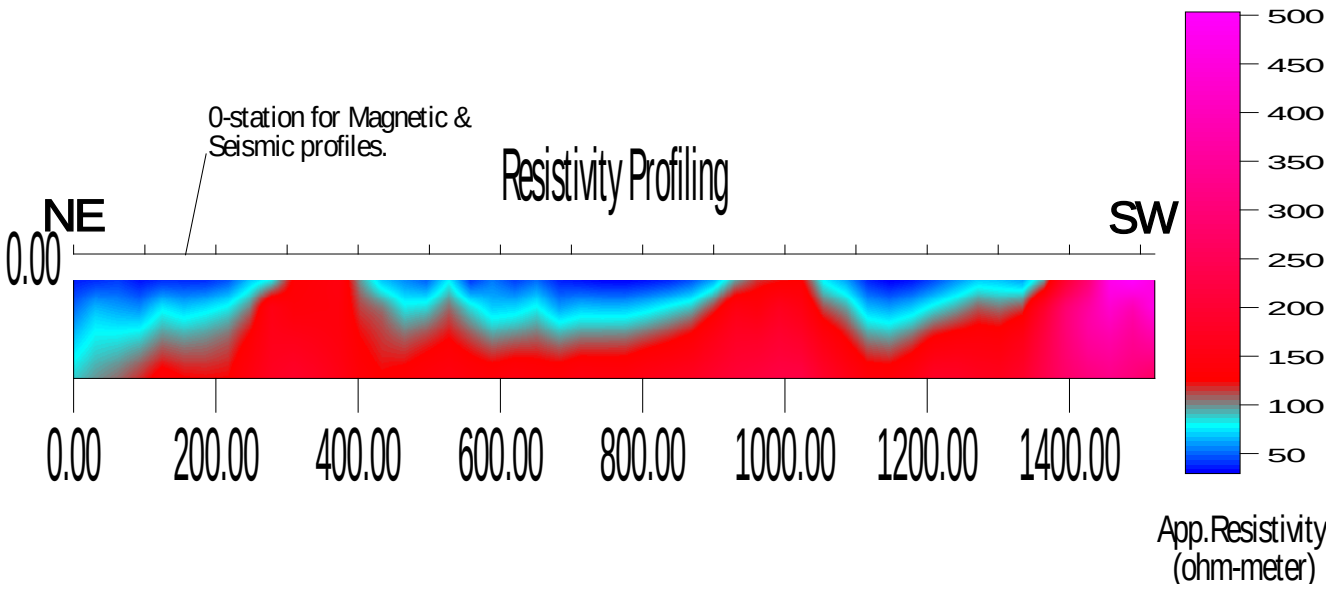

Fig 4.30 Apparent resistivty variation section

4.4.2.4 Results and Interpretations

The lateral apparent resistivty distribution of the profile at an electrode spacing of 20 m (Fig 4.29,a) shows relatively lower resistivty values of 30 to 40 ohm-meters at the first 240 meters distance, from 480 to 940 meters, and between distances of 1140 and 1380 meters along the profile. While the rest of the profile is marked by relatively higher resistivty responses for the same depth range.

From the geologic information, the lower resistivty values for the first 240 meters distance are associated with the shale-limestone-marl intercalation rock unit. Whereas from the distance 480 m to 940 m and between 1140 and 1380 meters are interpreted as the effect of water in the river and inside the soil respectively.

The relatively higher values of 146 ohm-meter, between the stations of 260 and 480 meters are due to the limestone exposure near to the surface. The values ranging from 115 to 132 ohm-meter, between station 940 and 1140 meters, are due to the effect of dolerite near to the surface. The maximum apparent resistivty value of 588 ohm-meter is observed at the end of the stations on the top of the dolerite ridge. This could be due to the dolerite outcrop on the surface.

At station 27 (540 m distance), where the curve shows a relatively higher value of 94 ohm-meter, is interpreted as the presence of shear zone or fault. This is directly correlated with the magnetic profiling (Fig 4.21).

For the electrode spacing of 40 m in Fig 4.29 (b), the curve shows similar lateral variations to that of the 20 m electrode spacing. But all the apparent resistivty values for each stations in fig 4.29 (b) (except at the end of the profile) show higher values comparing to each of the stations in Fig 4.29(a). This is interpreted as at higher depths the effect of the water decreases thus the apparent resistivty increases.

But inversely, the values at the end of the profile decrease to 470 ohm-meter (in Fig 4.29, b) from 588 ohm-meter (in Fig 4.29,a). The higher value in Fig 4.29(a) could be due to the presence of unsaturated porosity, which may be because of fracturing and weathering of the dolerite rock outcropped near to the surface.

At the electrode spacing of 100 m in Fig 4.29(c), almost relatively there is no lateral variation. But the over all values of the curve increases (rises) to an average of 200 ohm-meter comparing

to the curves in Fig 4.29(a) & (b). And at the end of the profile the highest values at Fig 4.29(a) and (b) relatively decreases in Fig 4.29(c). This implies that at higher depth of the area, almost there is the same rock formation along the whole profile.

The relatively lower values at stations 4 and 11 observed in the 100 m electrode spacing curve may be due to the presence of water inside a fracture.

All these interpretations are directly correlated to the geology, seismic, and magnetic results. Therefore, from the image section (Fig 4.30), which is an overlapped result of the three curves in fig 4.29, the following general interpretations are made about the area beneath the profile.

1) The lower apparent resistivty values (less than 100 ohm-meters) are interpreted differently at different places. At the first 200 meter it could be due to the shale rock unit or saturated zone. But the first interpretation is better for the author of this thesis using the information from the geology of that area. And that of between 500 & 900 m, and between 1100 and 1300 meters are due to the shallow water saturated zone. This is confirmed by the refraction seismic interpretation in profile-1.

2) The higher apparent resistivty values (ranging between 100 and 300 ohm-meters) are interpreted for the massive rock units in the area such as the limestone and the dolerite.

3) In the apparent resistivty section Fig 4.30, the difference in contrast between the lower and higher resistivty zones is interpreted as follows. In the case of the first 200 m it shows less contrast than that of at 500 to 900 and 1100 to 1300 meter distances. This could be due to the fact that the rock layer beneath the lower resistivty zone is more homogeneous than that of beneath the first 200 m. Of course, from the seismic section it is interpreted as a dolerite rock underlain to the saturated zone.

4) The very highest apparent resistivty value (greater than 300 ohm-meter), which is observed near to the surface over the dolerite rock unit, is due to the increasing of unsaturated porosity that may be because of fracturing and weathering near to the surface.

CHAPTER-5 CONCLUSIONS AND RECOMMENDATIONS

5.1 Conclusions

The following conclusions have been drawn using the integrated approach.

1. As shown from the results of the integrated geophysical surveys, the area is highly affected by fracturing and faulting. Most of the detected fractures and faults are aligned along NW –SE strike directions similar to the regional structures. In the study area geologic boundaries and vertical contacts are also detected. Most of the limestone rocks near the contacts are highly fractured and tilted away from the nearest dolerite outcrops caused by the intruding dolerites. Consequently the limestone rock unit is highly affected by fracturing than the dolerites.

2. From the geological and integrated geophysical works, almost in every part of the study area there is a dolerite rock by forming either a dyke or a sill. The large volume of dolerite is exposed on the northern and southern margins of the studied area as dykes. And from the shallow refraction seismic results and the borehole log data the dolerite is intruded as a sill on the central part of the area. Most of the outcrops of the dolerites are found associated with the fractures and faults. This implies that the intrusion took place along weak zones. Thus, the faults and fractures are relatively older in age than that of the dolerites.

3. The geological structures (fractures, faults, and contacts) play a great role in the movement and occurrence of the groundwater in the study area. At the river course mostly

near the geophysically inferred and detected fractures, water starts to appear and flow along the river. Along the river course, which is otherwise dry, water gushes out at the dolerite-limestone contact and accumulates at the upstream side of the dolerite outcrop. However, at the downstream side of the outcrop it is all dry since the outcrop continues further down. It is therefore concluded that the fractured limestone and its horizontal bedding contributes more for the recharge and movement of the groundwater next to the faults and weak zones. Where as the dolerite acts as a barrier for the groundwater flow.

4. In this shallow subsurface exploration geophysics of hard rock terrain, it is almost impossible to detect the groundwater table, which is found at depths greater than 40 meters. The exception to this is found in the southeastern part of the study area, where shallow saturated zone is detected using the seismic refraction and resistivty profiling at 5 to 20 meters depth on the dolerite along the fractures covered by a thick soil deposit. Probably this is a better place in case additional drilling for productive well sites are needed. Most of the existing wells are near to the detected fractures and weak zones except PW-6 and PW-7, which were drilled on 20 to 35 m thick limestone. These wells would have been more productive if they were drilled exactly on the detected fractures and weak zones.

5.2 Recommendations

Based on the outcomes of this study, the following recommendations are forwarded.

1. The fractures and weak zones are the major reservoirs for the groundwater in that area with hard rock terrain. There is no other place for groundwater storage better than these geologic structures. Thus if a need arises for drilling productive groundwater wells it would be better along the geophysically detected faults and weak zones. The second choice will be, on the contacts between the downstream dolerite and the upstream limestone outcrops.

2. Most of the existing wells in the study area are densely concentrated along only one side (northern side) of the river. This causes depletion of the groundwater along one side of the river. Thus additional drilling along this same side of the river should be avoided.

3. In order to map the networks of fractures and faults additional geophysical methods are recommended with profiles perpendicular to the ones taken in this study.

REFERENCES

Abedlwassie Hussein, 2000, Hydrogeology of the Aynalem Wellfield, Tigray, Northern Ethiopia.

Alfonso B., Antonio R.,Pier L.F., Getaneh A. and Tadesse S., 1997, The Mesozoic Succession of the Mekelle outlier (Tigray Povince, Ethiopia), Padova.

Beyth, M., 1970, explanatory notes-Mekelle sheet ND37-11, Geological Survey of Ethiopia

Beyth, 1972, The geology of Central-Western Tigray, Geological Survey of Ethiopia.

Beyth M. & E.Shachnai, 1970, Hydrogeology of Mekelle area, Geological Survey of Ethiopia.

Burger H. Robert, 1992, Exploration Geophysics of the Shallow Subsurface, Prentice Hall PTR, New Jersey.

Dainelli G., 1943, Geologia dell'Africa Orientale Vol. I-III. Roma.

Dobrin, M.B, 1976, Introduction to Geophysical Prospecting, 3rd edition, McGraw-Hill, New York.

Edwards L.S., 1977, A modified pseudosection for resistivty and induced-polarization. Geophysics, 42, 1020-1036.

Levitte, D., 1970, The Geology of Mekelle, Report on the central part of sheet ND37-11, Geological Survey of Ethiopia.

Loke M.H., 1999, Electrical Imaging Surveys for environmental and engineering studies (A practical guide to 2-D and 3-D surveys).

Merla, G., and E. Minucci, 1938, Missione geologica nel Tigrai: Rome, Reale Accad.Italia,362 P.

Milsom, John, 1989, Field geophysics, Geological Society of London handbook, John Wiley & Sons.

Palmer, Derecke, 1980, The generalized reciprocal method of seismic refraction interpretation: Tulsa, Oklahma, Society of Exploration Geophysicists, 104 P.

Redpath, Bruce B., 1973, Seismic refraction exploration for engineering site investigations: Technical report E-73-4, Explosive Excavation Research Laboratory, Livermore, California,51 p.

Robinson, E.S., & Coruh, C., 1988, Basic Exploration Geophysics, John Wiley & Sons, New york.

Shumburo M.M., 1968, The Amba-Aradam formation (formerly the upper sandstone) Mobile Petroleum Ethiopia Inc.

Telford, W.M., Sherif, R.E., & Geldart, L.P., 1980, Applied Geophysics, Cambridge University press, London.

Tesfaye Chernet & Gebretsadik Eshete, 1982, Hydrogeology of the Mekelle area (ND37-11), Ministry of Mines & Energy Ethiopian Institute of Geological Surveys.

WSSA, 1992, Water Resources Verification Report Mekelle.

APPENDIXES

Appendix-1 Seismic velocities for some common rocks after Mussett (2000)

Rock Type	V_p (km/sec)
Unconsolidated sediments	
Clay	1.0 – 2.5
Sand, dry	0.2 – 1.0
Sand, saturated	1.5 – 2.0
Sedimentary rocks	
Anhydrite	6.0
Chalk	2.1 – 4.5
Coal	1.7 – 3.4
Dolomite	4.0 – 7.0
Limestone	3.9 – 6.2
Shale	2.0 – 5.5
Salt	4.6
Sandstone	2.0 – 5.0
Igneous and Metamorphic rocks	
Basalt	5.3 – 6.5
Granite	4.7 – 6.0
Gabbro	6.5 –7.0
Slate	3.5 – 4.4
Ultramafic rocks	7.5 – 8.5

Others

Air	0.3
Natural gas	0.43
Ice	3.4
Water	1.4 – 1.5
Oil	1.3 – 1.4

Appendix-2 Magnetic susceptibilities of common rocks after Robinson (1988)

	SUSCEPTIBILITY x 10^6 emu	
TYPE	RANGE	AVERAGE
Sedimentary		
Dolomite	0-75	10
Limestone	2-280	25
Sandstone	0-1660	30
Shale	5-1480	50
Igneous		
Granite	0-4000	200
Rhyolite	20-3,000	
Dolerite	100-3000	1400
Gabbro	80-7200	6000

Basalt	20-14500	6000
Diorite	50-10000	7000
Peridotite	7600-15600	13000
Metamorphic		
Amphibolite	60	60
Schist	25-240	120
Phyllite	130	130
Gneiss	10-2000	
Quartzite	350	350
Slate	0-3000	500

Appendix-3 Resistivty of common earth materials after Robinson (1988)

Earth Material	Resistivty Ranges (ohm-m)
Unconsolidated sediment	
Sand	$1\text{-}10^3$
Clay	$1\text{-}10^2$
Marl	$1\text{-}10^2$
Sedimentary rocks	
Shale	$10\text{-}10^3$
Sandstone	$1\text{-}10^8$
Limestone	$50\text{-}10^7$

Dolomite	10^2-10^4
Crystalline rocks	
Granite	10^2-10^6
Diorite	10^4-10^5
Gabbro	10^3-10^6
Basalt	10-10^7
Schist	10-10^4
Gneiss	10^4-10^6
Slate	10^2-10^7
Marble	10^2-10^8
Quartzite	10-10^8
Groundwater	
Portable well water	0.1-10^3
Brackish water	0.3-1.0
Seawater	0.2
Super saline brine	0.05-0.2

Appendix-4 Well Logs of the Aynalem well-fields (after WWDE)

Well Name: **PB - 1** Casing Arrangement

Total Depth: 120 m Screen:

Water strike: Blank:

Static water level: 11.22 m

Depth,m	**Lithology**	**Description**
0-4	Clay	Sandy clay
4.0-15.0	Sand	Gravel sand, angular
15-25	Limestone	Highly weathered with marl/shale intercalation
25-45	Limestone	Highly weathered and moderately weathered
45-57	Sand	Sand fine grained, light in color
57-63	Limestone	Calcareous limestone

63-71	Limestone	Fractured limestone with shale intercalation
71-120	Dolerite	71-103 m massive dolerite 103-115 m highly fractured dolerite 115-120 m fresh dolerite

Well Name: **PB - 2**

Total Depth: 117.5 m *Screen:*

Water strike: *Blank:*

Static water level: 31.3 m

Depth,m	**Lithology**	**Description**
0.0--1.5	Soil	Clay soil
1.5-114	Dolerite	1.5-5 m highly weathered dolerite 5-11 m moderately weathered dolerite 11-38 m massive dolerite 38-44 m slightly fractured dolerite 44-109 m massive dolerite 109-114 m highly fractured dolerite

114-117.5	Limestone	Moderately weathered limestone

Well Name: **PB - 3**

Total Depth: 120 m

Water strike:

Static water level: 20.55m

Casing Arrangement

Screen:

Blank:

Depth,m	**Lithology**	**Description**
0-2	Soil	Sandy clay
2.0-45	Limestone	2-11m highly fractured, moderately weathered 11-29m highly weathered and fractured limestone with sub-angular gravel 29-33 gravely to sandy rounded and angular, poorly sorted limestone rocks 33-36 highly fractured limestone 36-35 highly fractured with calcite precipitation
45-120	Dolerite	45-51m fractured and slightly weathered

		51-88m massive dolerite
		88-92m highly fractured dolerite
		92-112m moderately fractured dolerite
		112-120m massive dolerite

Well Name: **PB - 4**

Total Depth: 120 m

Water strike:

Static water level: 15.15m

Casing Arrangement

Screen:

Blank:

Depth,m	**Lithology**	**Description**
0.0-2.0	Soil	Sandy clay soil
2.0-15	Limestone	2-11m highly weathered
		11-15m moderately weathered
15-21	Sandstone	Moderately weathered
21-31	Limestone	21-25m black limestone
		25-31 moderately fractured

31-120	Dolerite	31-37.5m moderately weathered
		37.5-49.5m fractured dolerite with calcite filling
		49.5-57.5m slightly fractured
		57.5-71.5m fresh dolerite
		71.5-73.5m slightly fractured
		73.5-77.5m fresh dolerite
		77.5-89.5m slightly fractured
		89.5-95.5m fresh dolerite
		95.-120 Slightly fractured at the bottom

Well Name: **PB - 5**

Total Depth: 104 m

Water strike:

Static water level: 13.33 m

Casing Arrangement

Screen:

Blank:

Depth,m	**Lithology**	**Description**
0.0-6.0	Soil	0-2m black cotton clay
		2-4m fine grained sand
		4-6m sandy clay

6-103	Dolerite	6-10m moderately weathered dolerite
		10-22m fresh dolerite
		22-24m fractured dolerite
		24-26m fresh dolerite
		26-30m fractured dolerite
		30-36m fresh
		36-40m fractured
		40-42m fresh
		42-44m fractured
		44-56m moderately fractured
		56-62m fine grained fresh dolerite
		62-68m moderately fractured
		68-70m fresh
		70-72m fractured
		72-74m fresh
		74-78m moderately fractured
		78-84m fresh
		84-88m moderately fractured
		88-92m fresh dolerite
		92-103m highly fractured
103-104	Limestone	Moderately weathered limestone

Well Name: **PB - 6** Casing Arrangement

Total Depth: 75 m *Screen:*

Water strike: *Blank:*

Static water level: 19.73 m

Depth,m	**Lithology**	**Description**
0.0-4.0	Soil	Sandy clay
4.0-35	Limestone	2-6m highly weathered sandy limestone 6-26m highly weathered sandy limestone and very white 26-35m black limestone
35-75	Dolerite	35-52m weathered dolerite 52-75m massive dolerite

Well Name: **PB - 7** Casing Arrangement

Total Depth: 65 m *Screen:*

Water strike: *Blank:*

Static water level: 8.01 m

Depth,m	Lithology	Description
0.0-2	Soil	Black cotton clay soil
2-10.0	Rock fragments	Rock fragments mainly limestone
10-20.0	Limestone	10-14m black limestone 14-18m fractured limestone 18-20m marl limestone , highly fractured with calcite precipitation
50-65	Dolerite	20-28m highly fractured dolerite 28-40m moderately fractured dolerite 40-65m massive dolerite

Well Name: **PB - 8**

Total Depth: 89.9 m

Water strike:

Casing Arrangement

Screen:

Blank:

Static water level: 19.31 m

Depth,m	Lithology	Description
0.0-2	Clay	Sandy clay
2.0-14	Limestone	2.0-10.0m weathered limestone white in color 10-14m black limestone
14-28	Shale	Dry shale
38-42	Rock fragments	Rock fragments mainly limestone, sandstone and shale
42-50	Limestone	Black limestone
50-62	Marl	Marl with calcite precipitation
62-89.90	Dolerite	Massive dolerite

Well Name: **PB - 9** Casing Arrangement

Total Depth: 71.5 m *Screen:*

Water strike: *Blank:*

Static water level: 16.26 m

Depth,m	**Lithology**	**Description**
0.0-8	Soil	0-2m black cotton soil 2-8m sandy clay
8.0-12	Rock fragments	Rock fragments mainly limestone
12.0-20	Shale	Dark shale
20-30	Shale/limestone	Shale with limestone intercalation
30-36	Gravel	Gravel from limestone formation
36-48	Siltstone	Siltstone
48-52	Sandstone	Sandstone

52-54	Gravel	Unsorted gravel
54-58	Limestone	Highly fractured limestone
58-70	Sandstone	Fractured sandstone
70-71.5	Dolerite	Massive dolerite

Well Name: **PB -10**

Total Depth: 98

Water strike:

Static water level: --

Casing Arrangement

Screen:

Blank:

Depth,m	**Lithology**	**Description**
0.0-2	Soil	Clay
2.0-8	Limestone	Highly weathered limestone
8.0-32	Limestone	Dark limestone

32-42	Siltstone	
42-48	Sandstone	
48-52	Dolerite	Weathered dolerite
52-98	Dolerite	Fresh dolerite

Well Name: **PB -11**

Total Depth: 75m

Water strike:

Static water level: 9.8m

Casing Arrangement

Screen:

Blank:

Depth,m	**Lithology**	**Description**
2.0-6	Clay	Sandy fine grained soil cover
6.0-62	Dolerite	6-8m highly weathered dolerite 8-12m moderately weathered dolerite 12-45m slightly fractured dolerite 45-52m massive dolerite

		52-62m highly fractured dolerite with calcite filling
62-66	Sandstone	Fractured sandstone
66-68	Dolerite	Fractured dolerite
68-73	Sandstone	Fractured sandstone
73 - 75	Dolerite	Massive dolerite

Well Name: **PB -12**

Total Depth: 85m

Water strike:

Static water level: 14.97m

Casing Arrangement

Screen:

Blank:

Depth,m	**Lithology**	**Description**
0.0-4	Clay	Sandy clay
4.0-20	Sandstone	Weathered sandstone with rock fragments

20-25	Limestone	Weathered limestone
25-30	Marl	Highly weathered marl
30-85	Dolerite	30-34m weathered dolerite 34-80m Fresh dolerite

Well Name: **DEBRI(MTW-1)** Casing Arrangement

Total Depth: 83.5 *Screen:*

Water strike: *Blank:*

Static water level:

Depth,m	**Lithology**
0.0-3	Black cotton soil
3.0-6.0	Marl clay
6-10.0	Shale with unconsolidated layer

39.51

10.0-18	Gravel sand with limestone pebbles
18-32	Shale with unconsolidated layer, the lower part fractured
32-36	Shale
36-50	Limestone with marl upper part fractured
50-52	Sand with gravel
52-54	Slightly weathered limestone
54-83.5	Non fractured black limestone